Journal of Geochemical Exploration xxx (xxxx) 107053

Contents lists available at ScienceDirect

Journal of Geochemical Exploration

journal homepage: www.elsevier.com/locate/gexplo

The Au–Ag (Zn, Pb, Mo, Cu) Sulfuro Vein, La Paloma district, Deseado Massif, Argentina: Geochemical characterization and new insights into the 4D evolution of ore shoots

María Lis Fernández [a, b, *], Marta Franchini [a, b], Stefano Mazzoli [c], Pablo J. Caffe [d], Alejandro Garrone [e]

[a] *Consejo Nacional de Investigaciones Científicas y Técnicas, Centro Patagónico de Estudios Metalogenéticos, Argentina*
[b] *Universidad Nacional del Comahue, Facultad de Ingeniería, Departamento de Geología y Petróleo, Buenos Aires 1400, Neuquén, Argentina*
[c] *School of Science and Technology, Geology Division, University of Camerino, Italy*
[d] *Universidad Nacional de Jujuy, Instituto de Ecorregiones Andinas (CONICET-UNJu) e Instituto de Geología y Minería, Jujuy, Argentina*
[e] *Universidad Nacional de Córdoba, Facultad de Ciencias Exactas, Fisicas y Naturales, Córdoba, Argentina*

ARTICLE INFO

Keywords:
Epithermal deposit
Structural and lithological control
Fluid chemistry
Metal zonation

ABSTRACT

Unravelling the 3D architecture of ore shoots and its evolution through time, thereby moving towards a 4D understanding of mineralization processes, requires an interdisciplinary approach based on the capability of carrying out extensive trenching and drilling as well as effectively integrating structural and geochemical analyses. Such conditions are offered in La Paloma district of the Deseado Massif, Argentina. Here, eight epithermal Au–Ag veins are hosted in Middle Jurassic volcanic rocks (Bajo Pobre Formation). The Au–Ag (Zn, Pb, Mo and Cu) Sulfuro Vein, representing the main ore body in the district, is a 750 m long, N to NW striking structure extending 230 m at depth. The geometry and distribution of ore shoots within the Sulfuro Vein are controlled by: (i) lithological and structural features, (ii) metal concentration, (iii) temperature of the fluids at the time of ore deposition, and (iv) remobilization processes. The highest values of Au, Ag, Cu, Mo, Pb, Zn and Sb are concentrated at depths between 50 and 100 m.a.s.l., while high Mo values occur also at greater depths in the southern segment of the vein. Molybdenum distribution in shallower sectors of the vein is controlled by its remobilization by later infill stages. The Au, Ag and Cu ore shoots are widely distributed in the southern and central segments of the vein, as are the areas of greater vein thickness. These ore shoots exhibit a sub-horizontal geometry consistent with dominant extensional faulting during mineralization. In the northern segment of the vein, the Au, Ag and Cu ore shoots are discontinuous and small, and show gentle to moderate plunges probably associated with variable fault kinematics and depletion of the fluid in these metals. Ore-shoots of Mo, Pb and Zn display high values along the longitudinal section and sub-horizontal geometry in the central and northern sectors of the vein, with high-grade Mo ore shoots decreasing to the north. The fact that Pb and Zn high grades extend up to the tip of the northern vein segment suggests that these metals continued to precipitate at lower temperatures, favoured by the permeability of the volcaniclastic units. All of the ore shoots exhibit steeper plunges towards the southern termination of the vein. Here, upward fluid flow may have been enhanced by the dilation associated with oblique-slip along the N-S striking segment of the steeply dipping Sulfuro Vein. The geochemical distribution of metals shows a slight vertical zonation and a distinct lateral zonation, which suggest hydrothermal fluids flowed northward from deeper zones in the southern sector of the vein.

1. Introduction

Numerous studies discuss the structural controls, wall-rocks influence (competence, permeability contrast and chemical reactivity) and fluid pressure gradients, on the fluid pathways and high-grade ore-shoots location in epithermal fault-vein networks (e.g. Cox et al., 2001; Cox, 2005; Simmons et al., 2005; Squire et al., 2008; Micklethwaite, 2009). However, no recent studies have been conducted to understand

* Corresponding author at: Centro Patagónico de Estudios Metalogenéticos, Universidad Nacional del Comahue, Facultad de Ingeniería, Departamento de Geología y Petróleo, Buenos Aires 1400, Neuquén, Argentina.
E-mail address: marialisfer@gmail.com (M.L. Fernández).

https://doi.org/10.1016/j.gexplo.2022.107053
Received 8 January 2022; Received in revised form 30 May 2022; Accepted 27 July 2022
0375-6742/© 20XX

how these factors interact throughout the history of vein infill and lead to ore-shoot formation. Carrying out this type of study involves obtaining a 3D comprehensive picture of ore concentration and vein thickness for a mineralized rock volume, a kind of information that is not easy to obtain in many instances. A thorough multidisciplinary study integrating detailed fieldwork, acquisition and processing of geophysical data, and extensive drilling as well as a large amount of laboratory work including coupled drill-core and geochemical analyses are required to accomplish such a task. The Au ± Ag (Zn, Pb, Mo, Cu) Sulfuro Vein of the La Paloma district, situated in the NE sector of the Deseado Massif, Argentina (Fig. 1a), provided a unique opportunity to carry out such an integrated study. In this paper, we report 3D architecture of the mineralized vein in terms of both geometrical parameters and ore contents. The results allowed us to obtain information also on the progressive, multiphase development of the ore body, thus providing useful insights onto the 4D evolution of ore shoots. Our study will hopefully contribute to better understanding of how lithological and structural controls, besides fluid chemistry and metal remobilization, influence the generation of ore shoots in epithermal environment.

The Sulfuro Vein constitutes the highest-grade mineralized structure of La Paloma, with a measured resource of 174.251 Oz of gold and 525.985 Oz of silver and an average grade of 6.6 g/t Au and 20 g/t Ag (Garrone, n.d.; unpublished results), representing about 65 % of the total measured resources of the district. This contribution presents the first paragenetic sequence, the correlations and associations between metals and their distributions in a longitudinal section of the Sulfuro Vein. Structural and lithological data from vein and geochemical data modelled in 2D representations are combined using the Leapfrog Geo software that integrates surface and subsurface information. As such, 2D representations include information on the third dimension in the form of vein thickness contours (coupled with ore concentrations), the information they convey is fully three-dimensional. We also apply the results obtained from a previous structural analysis (Fernández et al., 2020) combined with geochemical analysis, vein infilling mineralogy and textures, in order to unravel the geometry and distribution of ore shoots within the Sulfuro Vein. The combination of structural, lithological, mineralogical and geochemical information provides new insights into the morphology of ore shoots and constitutes a useful tool in unravelling the paleo-direction of hydrothermal fluids, which may be used as a guide for future exploration activities in the district and elsewhere.

2. Regional geology

The Deseado Massif of southern Patagonia of Argentina (Fig. 1a) contains numerous Jurassic Au—Ag epithermal deposits (Schalamuk et al., 1997, 1999; Guido and Schalamuk, 2003; Echavarría et al., 2005; Fernández et al., 2008) with a metal endowment of almost 30 million ounces gold equivalent (Moz Au eq.) and eight currently active mines (Fernández et al., 2008; Guido and Jovic, 2019; Secretaría de Minería Argentina, 2022).

Metamorphic basement rocks of Neo-Proterozoic to Late Paleozoic (Carboniferous) age (Di Persia, 1962; Viera and Pezzuchi, 1976) crop out occasionally in the Deseado Massif (Fig. 1a) and are generally covered by Late Permian *syn*-rift and Triassic sag basin successions. The

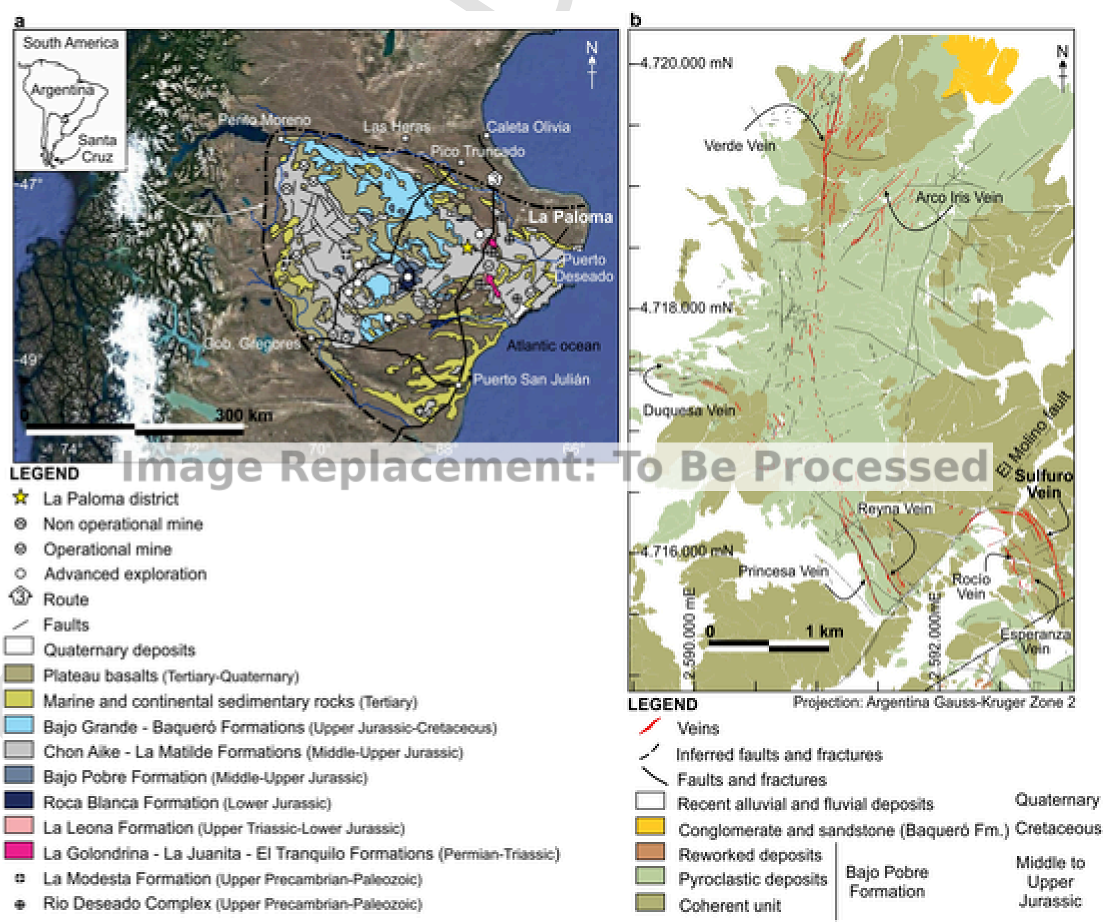

Fig. 1. a Regional geologic map of the Deseado Massif showing the location of the study area (yellow star), operational and non-operational mines and epithermal deposits in advanced exploration (modified from Ramos, 2002; Guido et al., 2004). **b** Simplified geological map of La Paloma showing major veins, faults and fractures in the district. (For interpretation of the references to colour in this figure the reader is referred to the web version of this article.) (For interpretation of the references to colour in this figure legend, the reader is referred to the web version of this article.)

earliest magmatic event is represented by Late Triassic-Early Jurassic granitoids of the La Leona Formation (Arrondo, 1972) which intrude the Permian to Triassic sedimentary rocks and have been interpreted as the south-easternmost outcrops of the Central Patagonia Batholith (Rapela and Pankhurst, 1996; Rapela et al., 2005). These rocks are overlain by Middle to Upper Jurassic volcanic and volcaniclastic rocks of the Bahía Laura Volcanic Complex (BLVC) (Guido, 2004; Sruoga et al., 2008). The latter resulted from a volcanic mega-event that occurred in Patagonia, giving rise to the Chon Aike Silicic Large Igneous Province (SLIP) (Pankhurst et al., 1998, 2000; Riley et al., 2001). The formation of the SLIP occurred during the early break-up of western Gondwana and rifting due to crustal weakening related to a single mantle thermal anomaly, known as Karoo mantle plume (Navarrete et al., 2019; Folguera et al., 2020, and references therein). The volcanism represented by the BLVC (V2 event of Pankhurst et al., 2000) was bimodal, although acid compositions and related pyroclastic rocks predominate. The geological relationships and radiometric ages indicate that mafic and felsic magmatism were coeval and overlapped in space and time during most of the volcanic episode (Dietrich et al., 2012; Wallier, 2009). The volcanic rocks of the Bajo Pobre Formation and the subvolcanic intrusions of the Cerro Leon Formation are andesite and basaltic andesite in compositions (Guido et al., 2004, 2006). The felsic units comprise rhyolitic to rhyodacitic pyroclastic sequences with subordinated epiclastic deposits and intercalated lava flows (Pankhurst et al., 1998) of the Chon Aike Formation and fossiliferous lacustrine epiclastic rocks of the La Matilde Formation (Pankhurst et al., 1998).

The Jurassic formations are overlain by Cretaceous continental deposits of the Bajo Grande and Baqueró formations (Archangelsky, 1967; Archangelsky and Cuneo, 1984; Hechem and Homovc, 1988). Cenozoic marine and continental sedimentary rocks and extensive basaltic flows partially cover the Jurassic and Cretaceous units (Gorring et al., 1997; Panza and Franchi, 2002).

According to geochronological data (Arribas et al., 1996; Dubé et al., 2000; Wallier, 2009; Dietrich et al., 2012; Permuy Vidal et al., 2016; Mugas Lobos et al., 2021), hydrothermal activity occurred during restricted episodes of the intense volcanism in the Middle and Late Jurassic. This resulted in the formation of veins, hydrothermal breccias and stockworks that were emplaced in the epithermal environment hosting Au/Ag and polymetallic epithermal deposits in the Deseado Massif (Schalamuk et al., 1997, 1999; Guido et al., 2005; Jovic et al., 2011; López et al., 2015). Surface hot spring manifestations were also formed in the geothermal environment related to the Late Jurassic hydrothermal activity (Guido and Schalamuk, 2003; Guido and Campbell, 2011).

Ore deposits throughout the Deseado Massif are regionally controlled by dominant NW and WNW-striking dilatational and hybrid fault-fracture networks, respectively. These formed in response to a regional tectonic regime characterized by bulk NE-SW-trending horizontal extension during the Jurassic in the Deseado Massif (Giacosa et al., 2010). However, local variations of the structural trends have been documented in other areas of the massif (Echavarría et al., 2005; Giacosa et al., 2010; Páez et al., 2016), and also in the area of the present study (Fernández et al., 2020) in response to inherited structures in the host rock.

3. La Paloma district

3.1. District geology

The Jurassic volcanic rocks of the Bajo Pobre Formation represent the oldest and extensive outcrops at La Paloma and hosts the studied epithermal veins (Fig. 1b). The Bajo Pobre Formation comprises three main lithological groups: (1) lavas and intrusive rocks, (2) pyroclastic rocks, and (3) reworked volcaniclastic rocks. The first group, composed of andesite to basaltic-andesite coherent and autobrecciated flows as well as shallow subvolcanic (stocks and laccoliths) intrusions, is the most representative in the district. Pyroclastic rocks are either intercalated between andesitic lava flows or intruded by basaltic-andesite stocks and laccoliths. Pyroclastic sequences can be interpreted as surge and pyroclastic flow deposits that commonly show strong facies variations and lateral change of thickness. Laminated to massive surge deposits are extensively distributed in the Sulfuro Vein and Princesa and Reyna sectors. They are less abundant in the Arco Iris and Verde veins areas, in which appear as thin laminated horizons intercalated between pyroclastic flow deposits of massive and chaotic fabric. The latter crop out extensively in the northern portion of the district, in the Arco Iris, Verde and Duquesa veins sectors. Reworked volcaniclastic sequences comprise debris and hyperconcentrated flow deposits scarcely preserved that overlay primary volcanic units or are subordinately intercalate between them. This kind of deposits seems to be restricted to topographic highs in the southern and eastern areas of the Sulfuro Vein and in the Duquesa Vein region. Extensive outcrops of the Chon Aike Formation comprising lava flows, domes and rhyolite to rhyodacite dikes are predominant at the southwest La Paloma district; they seem to be controlled by NE oriented structures in their contact with the rocks of the Bajo Pobre Formation. In the northern sector, Cretaceous sedimentary rocks ascribed to the Baqueró Formation represent the top units of the local stratigraphy, being locally overlain just by recent alluvial and colluvial sedimentary deposits that partly mantle the Mesozoic sequence.

The La Paloma district displays a complex vein network dominated by NNW to NW (with local N-S and NNE deflections) striking major veins (i.e., Sulfuro, Esperanza, Rocio, Princesa, Reyna and Verde) ENE to *E*-W (Duquesa) and NE (Arco Iris)- striking structures. The NE-SW-striking El Molino fault separates the Sulfuro Vein System (Sulfuro, Esperanza and Rocio veins) from the remaining veins located towards the north-northwest of the district (Fig. 1b). Veins at La Paloma are hosted within normal and oblique-slip fault zones showing variable magnitudes of shear and dilation (hybrid extension-shear fractures). The detailed structural analysis carried out by Fernández et al. (2020) documented that NNW to NW-striking veins are associated with normal faults. They constitute the thickest structures, as well as those with the largest vertical and along-strike extent, with a multi-episodic sequence of ore infill and high metal contents. ENE to E-W-striking veins also show normal fault kinematics and form thick structures. They display smaller along-strike lengths with respect to the former, and document fewer opening-filling events represented by late pulses (E3) with lower metal contents than NNW to NW veins. The NE-striking vein systems, Arco Iris and El Molino, are associated with oblique-slip faults characterized by a normal dip-slip component combined with right- or left-lateral strike-slip components, respectively. These structures do not record significant opening, as almost barren cataclastic fault rocks characterize their infill.

At the present time, the mineral resources of La Paloma district come from the Sulfuro Vein System (Sulfuro, Esperanza and Rocio veins). This system has a measured mineral resource of 260,566 Oz of gold and 637,590 Oz of silver, and an average grade of 5.55 g/t Au and 13.58 g/t Ag (Garrone, n.d.; unpublished results) which is currently exploited by the mining company Cerrado Gold Inc. to obtain Au, Ag and other metals (Zn, Mo, Pb and Cu) as by-product.

3.2. The Sulfuro Vein

3.2.1. Lithology

Based on the bench mapping in quarries and drill core logging, Godoy Prieto and Palluzi (2020) defined at least three lava units, named A1, A2 and A3 andesites, and two volcaniclastic sequences that host the Sulfuro Vein (Fig. 2a). The basal A1 unit covers the north and south sectors of the Sulfuro Vein with a thickness of 125 to 190 m. Unit A1 comprises a predominantly coherent, flow foliated, dense to amyg-

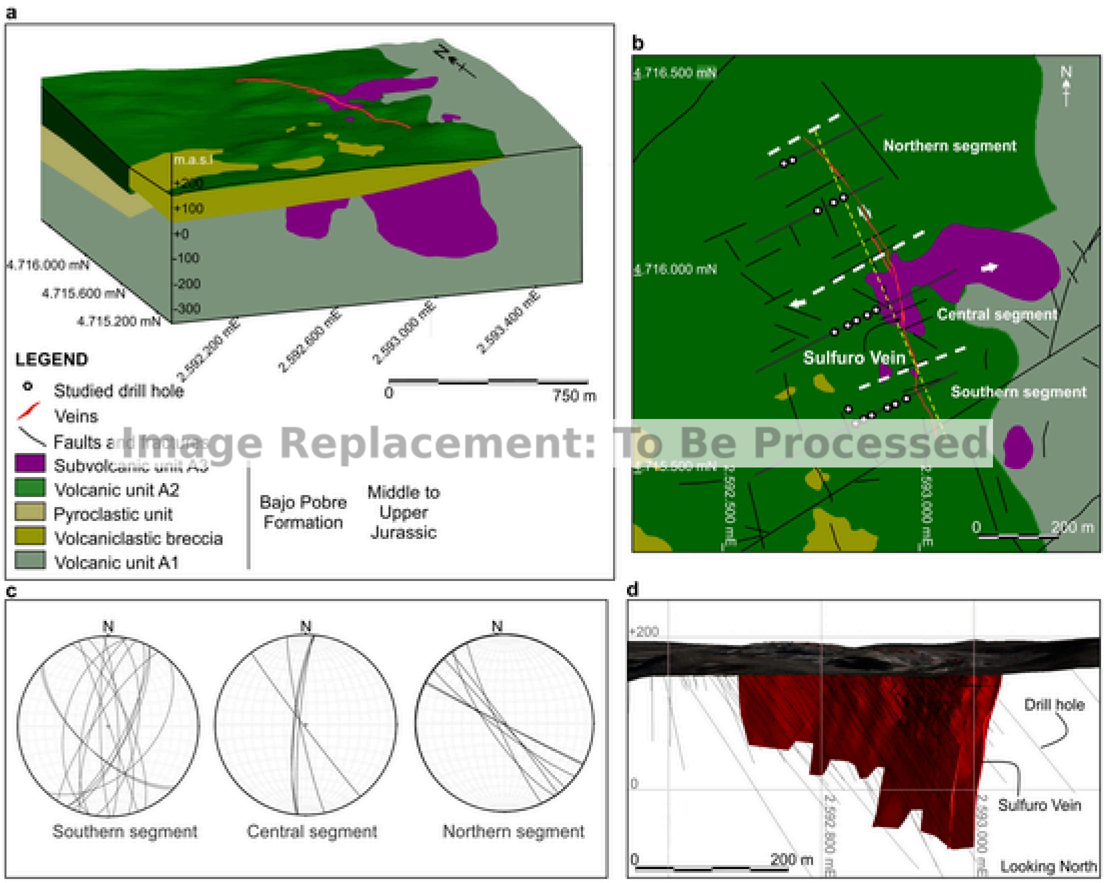

Fig. 2. **a** Schematic block diagram showing the lithology hosting the Sulfuro Vein from Leapfrog model. **b** Map view of the principal segment of the Sulfuro Vein analyzed in this study showing faults (black lines), host rock types and subdivision adopted in the study among the southern, central and northern segments (separated by coarse white dash lines). Bold white arrows show maximum extension direction obtained by stress inversion from a large fault-slip dataset (Fernández et al., 2020). The yellow dash line represents the trace of the longitudinal section used for Figs. 8,9 and 10. The location of studied drill holes along NE-SW cross-sections (dark grey lines) is also shown. **c** Lower hemisphere, equal area projections show orientation data (great circles) for fault and fracture planes measured from the three segments of the Sulfuro vein analyzed in this study. **d** 3D model of the Sulfuro Vein with the traces of drill holes. Black dot points show the position of composites used for modeling. (For interpretation of the references to colour in this figure the reader is referred to the web version of this article.) (For interpretation of the references to colour in this figure legend, the reader is referred to the web version of this article.)

dale-bearing porphyritic andesite with autobreccia intercalations. The top of this unit was only observed in drill cores. In the southern segment and in the southern part of the central segment of the Sulfuro Vein the A1 andesite is in contact with volcaniclastic breccias. In the northern segment and in the northern portion of the central segment, the A1 andesite is covered by pyroclastic surge deposits.

Pyroclastic rocks form continuous, tabular deposits up to 45 m thick in the central-north and north sectors (Fig. 2a), but in the central-south and south sectors they appear as discontinuous, lenticular blocks interfingered between lava flows from the A1 and A2 andesites (see below). There, pyroclastic and coherent volcanic units are cross-cut by dikes and intrusions from the A3 andesite event. Monomictic volcaniclastic breccias show chaotic, matrix-supported fabric, in which andesite lithic fragments that range from 3 cm up to 1 m in size, are included in a finer-grained matrix of the same composition. This lithofacies forms 40 to 80 m thick pseudo-tabular outcrops (Fig. 2a) interfingered with thinner horizons (<1 up to 8 m) ascribed to pyroclastic surge deposits.

Coherent lava flows corresponding to the A2 andesite unit lay above the sequence previously described in the three segments of the Sulfuro Vein (Fig. 2a). The A2 andesite is 15 to 20 m thick in the southern and central segments, doubling these values in the north. The A2 lavas are easily distinguished from the A1 andesites for the pinkish to reddish colour and the presence of a characteristic flow foliation that is stronger in the base; in that portion of the lava amygdales and interfingering of autobrecciated horizons are also common.

Dikes, stocks and laccoliths of basaltic andesite composition comprise the unit A3. These bodies cross cut the previous sequences in the central-south and southern segments (Fig. 2a). In some cases, these subvolcanic intrusions are injected following the orientation of flow foliation, or through the contact of volcaniclastic or pyroclastic sequences and the A2 andesite flows, acquiring sill-like shape.

3.2.2. *Structural features*

The Sulfuro Vein System (Sulfuro, Esperanza and Rocio veins) constitutes a ca. 1000 m long and up to 600 m wide block occupied by several segments of mineralized lodes between 0.3 and 6 m thick. This block is delimited to the north by the El Molino fault and to the south by a regional ENE- to NE-striking fault, which is interpreted to constitute the boundary of the Sulfuro vein (Fig. 1b). Although surface recognition of this major boundary fault is difficult, the integration of field mapping along with lineaments detected from satellite imagery and available geophysical data allowed us to infer its position. To the north, the Sulfuro Vein System turns to a WNW and then to an ENE strike that confers it an arcuate shape (Fig. 1b). South of such major deflection, the principal segment of the Sulfuro Vein analyzed in this study (Fig. 2b) shows a strike ranging from 300° to 357°N with local NNE deflections and displays a general western dip direction, with dip angles comprised between 75° and 90°N (Fig. 2c). The Esperanza and Rocio veins are subparallel to the Sulfuro Vein, but they show an eastern dip direction (mostly around 85°N). A large structural dataset is available in Fernández et al. (2020); the structural information provided in Fig. 2c represents a subset of such published data.

4. Analytical methods

Field data were collected by examination of approximately 2520 m of core from 17 selected drill holes from four cross sections across the deposit (Fig. 2b). One hundred and forty-six samples representative of the different epithermal infill types were selected from different depths in the deposit, based on hand specimen observations and access to geochemical data provided by Minera Don Nicolás S.A. The samples were analyzed first by binocular microscope and then by transmitted and reflected light microscopy. Petrographic data were complemented with standard scanning electron microscope (SEM) equipped with an energy dispersive X-ray analyzer, X-ray fluorescence (XRF) and X-ray diffraction analyses carried out to identify the nature, composition, texture and relative abundance of minerals in veins and breccias.

SEM examination of rock slabs and thin sections ($n = 5$) coated with carbon or gold, were made using a JEOL® JSM-IT500 scanning electron microscope (SEM) equipped with an energy dispersive X-ray analyzer (EDS, silicon drift detector Bruker) at the IC2MP Laboratory, University of Poitiers, France. SEM observations were made in secondary electron mode for morphological investigations and backscattered electron mode on thin sections for phyllosilicates chemical consideration. The analytical conditions included an acceleration voltage of 15 kV, a probe current of 1 nA, a working distance of 11 mm, and a counting time of 50 s per element. The standards used for EDS consisted of albite (Na, Al, Si), almandine (Mg, Fe), diopside (Ca), orthoclase (K), spessartine (Mn) and Ti metal (Ti). Matrix corrections were performed using the PhiRhoz mode (an evolution from ZAF methods) that is particularly efficient for light elements analysis.

A group of samples ($n = 10$) were selected for semi-quantitative geochemical analysis with micro-XRF mapping for ore mineral chemical characterization. Micro-XRF geochemical maps of thin section were produced on a Bruker M4 Tornado μXRF Energy Dispersive Spectrometer (micro-XRF EDS) using a 25 μm step size and 20 μm spot size with standard conditions of analyses at 3 ms/pixel, one frame count, operating at 40 kV acceleration voltage and 400 μA, at the University of New Brunswick, Canadá.

A first group of core samples ($n = 7$) was analyzed by X-ray diffraction on oriented preparation of the clay fraction (<2 μm) using a Rigaku DMAX-2D computerized equipment in the laboratories of the Universidad Nacional del Comahue and a Rigaku Smartlab in the Instituto de Geología y Paleontología of the Universidad Nacional de Rio Negro. The protocol used for the preparation of oriented mounts of clay material encompasses dispersion of clay particles in distilled water using ultrasonic probe, strontium saturation, separation of the <2 μm fraction size by sedimentation and/or centrifugation and preparation of oriented deposit on glass. XRD diffractograms of oriented preparations were acquired between 2 and 40° 2θ (CuKα1 + 2 radiation) in the air-dried state (AD), after solvation with liquid ethylene glycol (EG) and after heating 2 h at 550 °C. The diffractogram data of Moore and Reynolds (1997) were used to identify clay minerals. XRD analyses of another group of samples ($n = 12$) were made in the IC2MP Laboratory, University of Poitiers. The clay fraction (<4 μm) was extracted by grounding of pieces of rocks by wet milling in Mc Crone agate mill, sonification in water and then sedimentation. Diffractograms of oriented mounts were acquired using a Bruker D8 Advance diffractometer equipped with a detector linxeye and a Philips X'Pert Pro. Oriented mounts were analyzed in the air-dried state (AD) at room humidity and after solvation with ethylene glycol (EG) as a vapor in the range of 2–30° 2Θ, with CuKα1 + 2 radiation (40 kV and 40 mA).

Geochemical data for the Sulfuro Vein comes from exploration and ore-control drill holes and trenches provided by Minera Don Nicolás S.A. Out of a total of 2436 geochemical assay samples only 747 from 138 exploration drill cores and 39 trenches were assayed at 0.4 up to 1-m intervals through mineralized zones, for Au, Ag, As, Cu, Mo, Pb, Sb and Zn by conventional methods using ALS Chemex laboratory located in Mendoza (currently ALSglobal). The rest were assayed only for Au and Ag and were not included for the preparation of strike sections neither for the multivariate analysis methods. The geochemical models were developed using the Leapfrog Geo® 5.0 (licensed to MDN mining company) software which permits a 3-D display of geochemical data using a Radial Basis Function to create smooth surfaces from drill hole data samples, resulting in an interpolation of likely concentrations of elements between existing assays samples. Assay samples ($n = 747$) were composited to 1 m length using Datamine Studio RM software (licensed to MDN mining company) resulting in 549 composites (Fig. 2d). The coordinate of each composite is the midpoint of the from-to of the samples included in the composite using original coordinates (Gauss Kruger Faja 2).

Explorative statistical analysis was performed using the Pearson Correlation Coefficient (r) and Factor Analysis to measure the relationships between two or more random variables and to determine the ore-forming elements association, respectively. The Pearson Correlation Coefficient (r) measures the strength and direction of linear relationships between two or more random variables (Howarth and Sinding-Larsen, 1983; Paine, 1998; Bluman, 2003). It can range from −1 to +1, with −1 indicating a perfect negative correlation, +1 indicating a perfect positive correlation, and 0 indicating no correlation at all. In the present study r is used to investigate the relation between the metals analyzed in the vein (Au, Ag, As, Cu, Mo, Pb, Sb and Zn) and ranges were established to define low ($r = 0$–0.4), medium ($r = 0.4$–0.6), high ($r = 0.6$–0.9) and perfect ($r = 0.9$–1) correlations. Factor analysis was performed using Real Statistics software package supplemented with Excel to evaluate the association of elements within the geochemical data of the Sulfuro Vein. Principal component analysis was used to extract the number of factors that would represent the solution for the database analyzed and the Kaiser (1958) criterion was used as the factor retention criterion (eigenvalue >1.0). The number of extracted factors was corroborated by examination of the scree plot. The factor solution was rotated using the Varimax method to enhance the factor solution prior to interpretation (Davis, 2002; Hair et al., 2010). Variables were grouped to form factors according to the highest correlation (positive or negative) that the variable had with only one of the selected factors. Thus, variables can be associated with only one factor.

5. Results

5.1. Vein mineralogy and paragenesis

At the Sulfuro Vein multiple gangue and sulfide generations are grouped into twelve stages within three main episodes according to their mineralogy, metal contents, textures and crosscutting relationships (Fig. 3). The first episode (E1) consists of 6 stages and constitutes up to 70–80 vol% of the vein. The first stage (S1) is represented by a medium to coarse-grained quartz with rhombic adularia crystals (<50 μm) and pyrite (50–120 μm) (Fig. 4a) restricted to the deeper parts (−150 m.a.s.l) of the southern segment of the vein. The second stage (S2) (Fig. 4b) was only clearly observed in some parts of the northern segment of the vein and is represented by massive milky and grey microcrystalline quartz with kaolinite and disseminated fine-grained (<10 to 20 μm) pyrite. In the south and central parts of the vein this stage (S2) probably occurs as fragments enclosed by later vein stages, but its similarity with stage 4 makes it difficult to be sure about its occurrence within the paragenetic sequence. Stage 3 (S3) consists of 1 to 6 mm thick black to dark grey Au-bearing molybdenite-rich band

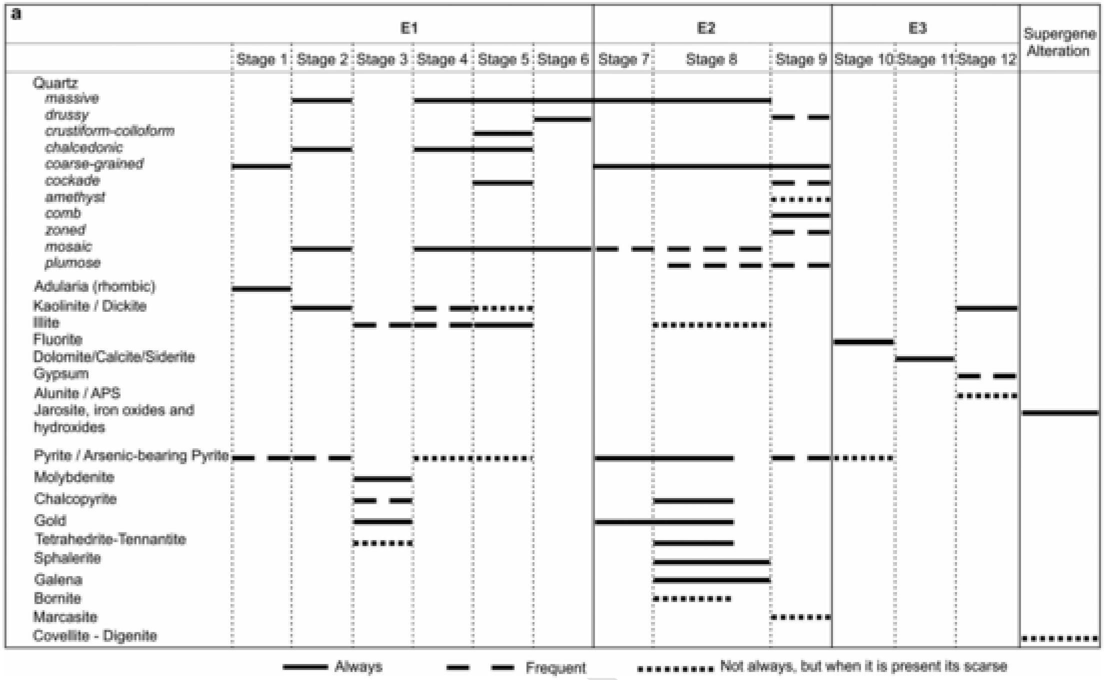

Fig. 3. Paragenetic sequence of hydrothermal infill minerals and ore of the Sulfuro Vein.

which often exhibits colloform-like texture (Fig. 4b - d). Stage 3 occurs commonly fragmented and cemented by minerals of later stages or as millimetric bands around clasts of wall-rock in brecciated texture style within the vein (Fig. 4c, d). In the deepest zones of the southern and central segments (< −25 m.a.s.l) and below 25 m.a.s.l. in the northern segment where this stage occurs in situ, S3 assemblages are in contact with the wall-rock (Fig. 4b). Molybdenite dominates and is associated with minor chalcopyrite and tetrahedrite-tennantite and illite (Fig. 4e, f). Sulfides are fine-grained (10 to 25 μm) except molybdenite which is notably coarser (up to 250 μm) in the deepest parts of the southern segment of the vein. Visible gold is seen in association with molybdenite and is also present as individual grains (< 15 μm) in contact with molybdenite and Cu-bearing sulfides (Fig. 4f - i). Gold anomalies related to this stage can reach up to 90 ppm Au. Stage 3 is followed by an extended, massive and crustiform-colloform banded quartz with phyllosilicates represented by stages 4 and 5 (Fig. 4b -d). Stage 4 consists of a massive grey microcrystalline quartz that typically occurs in contact with the molybdenite band (Fig. 4b - d) with minor amounts of kaolinite and illite (Fig. 4j, Tables A.1, A.2) and pyrite. Stage 5 constitutes the volumetrically most abundant infill of the Sulfuro Vein. It consists of massive but mainly crustiform-colloform banded, milky, beige, grey and light green quartz in hand specimen (Fig. 4c, d) with abundant illite and minor kaolinite (Fig. 4j, k; Table A.2). Bands of jasperoid quartz are locally present and alternate with previous bands (Fig. 4c). Commonly this stage forms cockade overgrowths around fragments of wall-rocks and vein (Fig. 4d). Stage 6 exhibits an identical distribution to the previous stage but is volumetrically minor. It consists of fine crystalline to microcrystalline, semi-translucent quartz with massive texture in hand specimen and numerous millimetric cavities where quartz increases in size and forms euhedral crystals (Fig. 4c).

The second episode (E2) consist of three stages which occupy 20–30 vol% of the vein represented by fine to coarse crystalline quartz and sulfides. Stage 7 was identified only in a few samples in the central part of the vein and consists of rhythmic millimetric bands (1 to 4 mm thick) of fine to coarse-grained crystalline quartz with disseminated pyrite that alternated with pyrite-rich bands (Fig. 4d). It also occurs as clasts cemented by later vein generations (Fig. 4c). Gold in this stage is microscopic (1.5 to 10 μm) and occurs in fractures and rims of pyrite crystals and interstitially between pyrite crystal aggregates (Fig. 5a). Stage 8 with pyrite ± sphalerite ± galena ± chalcopyrite ± tetrahedrite-tennantite and subordinate amounts of bornite is the main base metal stage. This stage shows a zonation in the distribution of sulfides, chalcopyrite and tetrahedrite-tennantite are dominant in the south and central sectors of the vein (Fig. 5b) and decrease towards the north, where sphalerite and galena are abundant (Fig. 5c, d). Pyrite is ubiquitous and is the most common sulfide in the vein. Stage 8 caused brecciation, as well as veins and veinlets that crosscut the previous pulses in the vein (Fig. 4d) and intruded into the wall-rock. Breccias range from jig saw-fit and clast-rotated to chaotic matrix-supported with subangular clasts of wall-rock and earlier vein infill. In the northern segment of the vein where this stage intercepts pyroclastic deposits, it replaces and cements the most permeable levels (Fig. 5d, e). It consists of coarse-grained sulfides (50 μm to 1 mm) which grade to zones of fine-grained sulfides (< 50 to 5 μm) disseminated in medium to coarse (50 to 150 μm) massive quartz with subordinate mosaic and plumose recrystallization textures. Illite and illite-smectite mixed-layer (Fig. 4j; Table A.2) is notably minor compared to episode E1 or is absent. Fragments of molybdenite were observed within this stage, probably remobilized from stage 2. Gold associated with stage 8 reaches values of 106 g/t Au and occurs as micro-inclusions (2.5 to 15 μm) within chalcopyrite (Fig. 5b, f), galena (Fig. 5g) and pyrite, in fractures within pyrite and interstitial between pyrite crystal (Fig. 5h). Stage 9 forms stockwork and individual quartz veinlets (0.5–15 cm) that cut the previous stages within the vein and the wall rock. It is volumetrically more significant in the deeper parts of the vein, where it commonly cements angular to subangular jigsaw-fit to rotated clasts of wall-rock and/or earlier vein stages (Fig. 4d, 5i). Quartz varies from medium to coarse crystals (< 2 mm) with comb textures and late drusy quartz and amethyst crystals filling voids. Individual crystals with zoned and plumose recrystallization textures are also common. This pulse contains pyrite (≤2 %) disseminated in quartz and in the central suture of the veinlets, in parts partially replaced by marcasite.

The third episode (E3) is post ore stage and marks the last event in the vein deposition sequence. It is represented by three barren stages with a wide distribution in the deepest zones of the vein, but is less important in terms of mineral volume. During E3 narrow veinlets (Fig. 5i) and cavities infill (Fig. 5j) within previous stages associations were formed. Stage 10 (S10) consists of purple, green and colourless fluorite

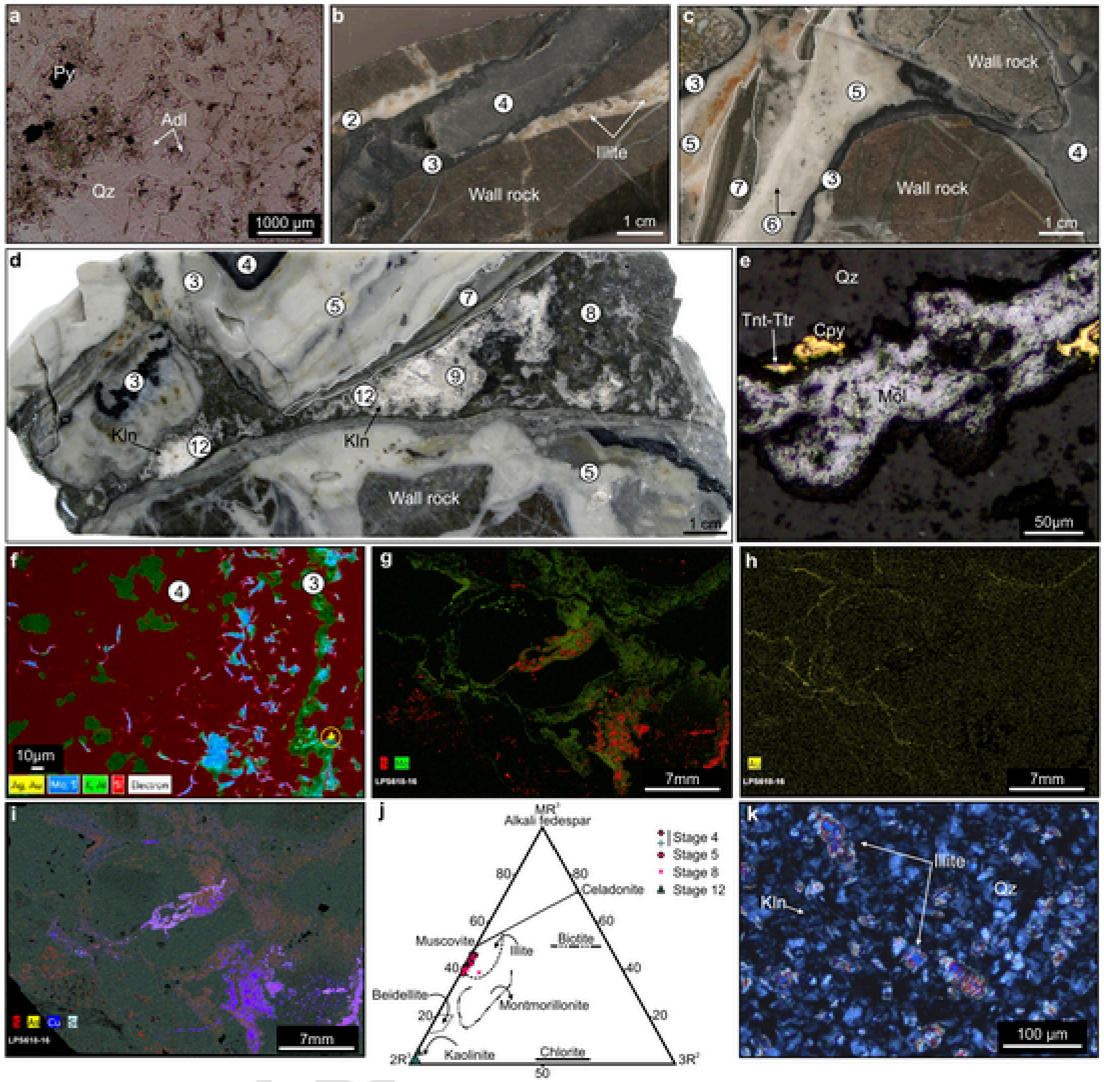

Fig. 4. Selected macro and microphotographs representative of vein infill stages presented in Fig. 3. **a** Microphotograph of stage 1 veinlet with rhombic adularia (Adl) crystals, quartz (Qz) and disseminated pyrite (Py). **b-d Selected** photographs representative of vein infill stages, textures and crosscutting relations at Sulfuro Vein (see text for details). Kln: kaolinite. **e** Microphotograph of a molybdenite (Mol) veinlet (stage 3) in contact with chalcopyrite (Cpy) and tennantite-tetrahedrite (Tnt-Ttr). Qz: quartz. **f** SEM-EDS compositional map shows **a** gold-bearing molybdenite band with illite. **g-i** Micro X-ray fluorescence (XRF) elements maps images show gold (Au) and copper (Cu) in a molybdenite-rich band (stage 3). **j** Plot of chemical composition of the hydrothermal clay minerals in the MR^3–$2R^3$–$3R^2$ triangle, in which silica is considered as a component in excess. MR^3 = Na + K + 2Ca; $2R^3$ = ([Al + Fe^{3+}] – MR^3)/2, and $3R^2$ = (Mg + Mn + Fe^{2+})/3 (Velde, 1985). **k** Microphotograph of illite, kaolinite (Kln) intergrown with quartz (Qz) (stage 5). (For interpretation of the references to colour in this figure legend, the reader is referred to the web version of this article.)

(Fig. 5i) and stage 11 (S11) is represented by calcite, dolomite and minor siderite (Fig. 5i). Gypsum, kaolinite ± dickite (Fig. 4j; Table A.1) and minor alunite and aluminum phosphate-sulfates (APS) with pseudocubic morphologies constitute the last stage (S12) (Fig. 4d, 5i, j). The crystallinity of kaolinite (from XRD, Table A.3), it's very low to nil iron content (Table A.1) and euhedral morphology (Fig. 5j) indicate a hydrothermal origin.

Between 5 and 15 m below the surface the vein is affected by a zone of supergene alteration with abundant iron oxides and hydroxides, jarosite and dissolution cavities (Fig. 5k). At the deepest levels and along fracture zones, scarce covellite and digenite replace chalcopyrite, bornite and tennantite-tetrahedrite along rims and crystals microfractures (Fig. 5l).

5.2. Geochemical characterization and metals distribution

Precious and base metal (Zn, Pb, Mo and Cu) mineralization in the Sulfuro Vein has a strike length of 750 m and extends to a depth of 230 m from the surface which is coincident with the maximum depth drilled. It has an average width of 2.9 m, reaching a maximum of 6 m, with a Ag:Au ratio ~ 6:1.

Pearson's correlation coefficient applied to the metal concentrations dataset is presented in Table 1. Gold shows weak positive correlation with the analyzed elements, however, the correlation factor is slightly higher with Ag, As, Cu and Sb. Moderate positive correlation was determined between Ag, Cu and Sb and high positive correlation between the last two. Copper shows weak positive correlation with the rest of the analyzed elements except with As which is moderate. Arsenic and Sb show moderate positive correlation between them. Molybdenum shows weak positive correlation with all the elements; however, the correlation factor with Au and Sb is slightly higher than with the rest of the elements. Lead shows perfect positive correlation with Zn.

Three factors with eigen values >1.0 were selected, providing 70.74 % of the total variance in the dataset with 37.49 % for factor one, 20.68 % for factor two and 12.57 % for factor three (Fig. 6a). All variables in the factor analysis were used to construct a scatter plot (Fig.

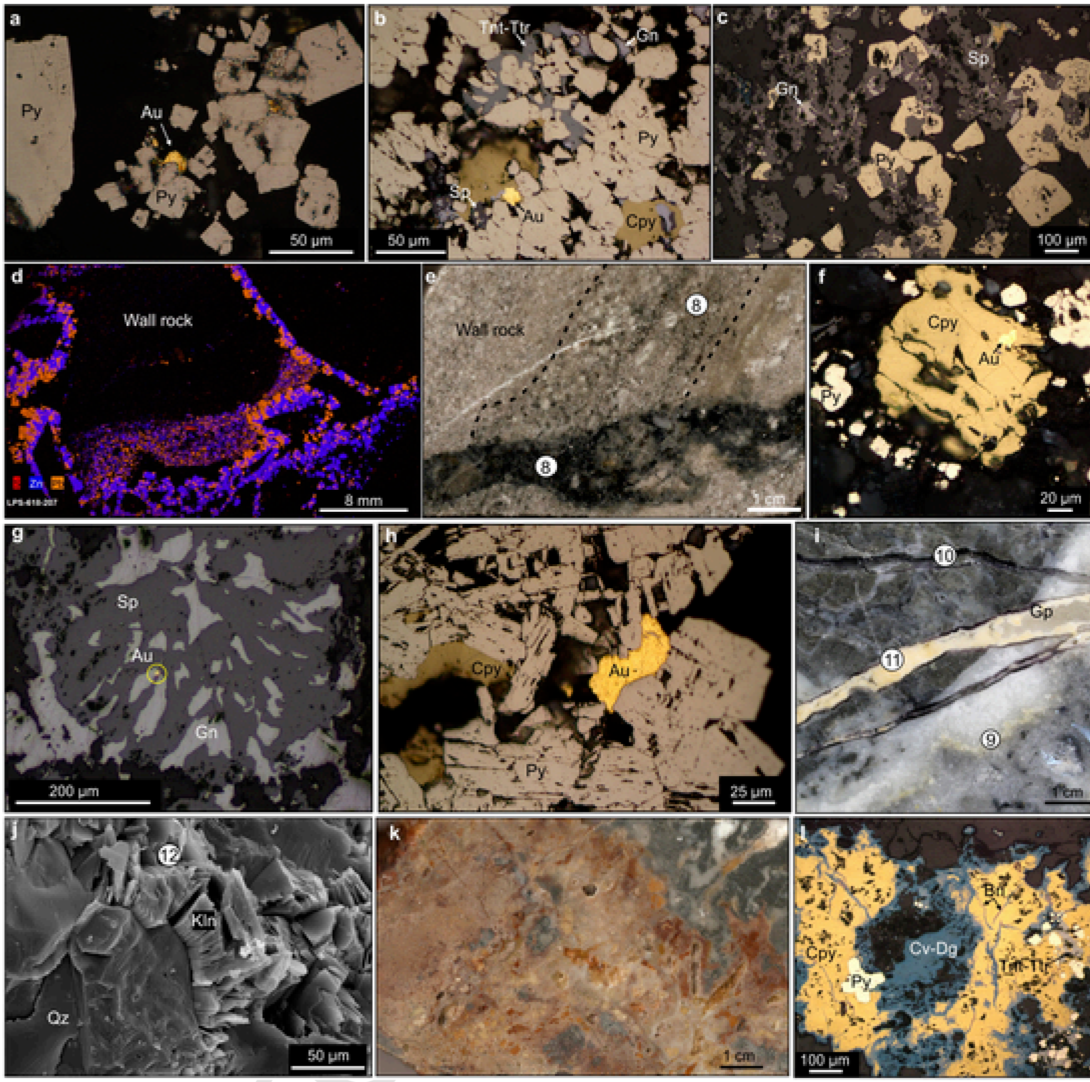

Fig. 5. Selected macro and microphotographs of gangue, precious and base metal mineralization of episodes E2 and E3 in the Sulfuro Vein. **a** Interstitial gold (Au) between pyrite (Py) aggregates (stage 7). **b** Interstitial chalcopyrite (Cpy), tennantite-tetrahedrite (Tnt-Ttr) and minor sphalerite (Sp) and galena (Gn) partially replace and fill voids in pyrite (Py) aggregates (stage 8). Gold (Au) micro-inclusions within chalcopyrite (Cpy). **c** Anhedral sphalerite (Sp) and galena (Gn) aggregates fill voids and partially replace pyrite (Py) crystals (stage 8). **d** Micro X-ray fluorescence (XRF) elements map image show permeable pyroclastic unit (wall rock) in the northern segment of the vein cemented by sphalerite (blue) and galena (orange) (stage 8). **e** Sulfide-rich veinlet in laminated pyroclastic unit (wall rock) with disseminated sulfides in coarser grained layers (stage 8). **f-g** Gold (Au) micro-inclusions within chalcopyrite and galena in mineralized samples (stage 8). **h** Interstitial gold (Au) between pyrite (Py) crystals (stage 8). **i** Photograph shows crosscutting relationships between stage 9 and stages 10, 11 and 12 in episode E3. Fluorite (Fl) veinlets (stage 10) reopened by calcite and dolomite (stage 11). Gypsum (Gp) (stage 12) fills open space within carbonate veinlet. **j** Backscattered image shows book like habit of kaolinite crystals that fill cavities between quartz (Qz) (stage 12). **k** Photograph representative of the supergene alteration. **l** Covellite (Cv) and digenite (Dg) after chalcopyrite (Cpy), bornite (Bn) and tennantite-tetrahedrite (Tnt-Ttr). (For interpretation of the references to colour in this figure legend, the reader is referred to the web version of this article.)

6b). The results of the Factor Analysis are shown in Table 2. Communalities represent the common factor variance extracted from each element, with a higher value indicating a better explanation of variables. According to the results, Factor 1 (F1) is dominated by Ag, As, Cu and Sb. Factor 2 (F2) consist of Pb and Zn and factor 3 (F3) was dominated by Mo and Au.

The contents of Au, Ag, Cu, Mo, Pb, Zn, As and Sb were analyzed as a function of depth (Fig. 7). The highest contents of precious and base metals were recognized between 50 and 100 m.a.s.l. (meters above the see level) except for As which is more abundant between 100 and 150 m.a.s.l. Silver and Au contents decrease from 50 to 100 m towards the surface and with depth; at depths >150 m.a.s.l. only Au anomalies were identified (Fig. 7a). The highest Cu, Pb and Zn contents are between 0 and 150 m.a.s.l., with the highest values corresponding to Pb and Zn (Fig. 7b). Although the highest Mo contents are located between 50 and 100 m.a.s.l., high values are also found in deep levels and are open below −50 m.a.s.l (Fig. 7c). The highest Sb and As concentrations occur at shallow depths, between 50 and 150 m.a.s.l. Arsenic values are higher than Sb and such difference is more pronounced at shallow levels, except between 50 and 100 m.a.s.l. where Sb contents exceed As (Fig. 7d).

Fig. 8 illustrates metal distribution (Au, Ag, Cu, Mo, Pb y Zn), Sb/As values, vein thickness variation, geometry of ore-shoots and the base of the supergene alteration zone in the longitudinal section of the Sulfuro Vein shown in Fig. 2b. For the analysis of metal concentrations, the vein was divided into three segments (southern, central and northern; Figs. 2b; 8) delimited by the ore-shoot size and geometry and/or by the NE to ENE faults crosscutting the vein.

High Au values occur in ore-shoots (>5 ppm Au) that can reach very high grades (up to 240 ppm Au) and crop out in the central and

Table 1
Pearson's correlation coefficient (r) matrices between metals in the Sulfuro Vein. Moderate correlations are in bold, high correlations in bold and italic, and perfect correlations in bold and underline.

	Au_ ppm	Ag_ ppm	As_ ppm	Cu_ ppm	Mo_ Ppm	Pb_ ppm	Sb_ ppm	Zn_ ppm
Au_ppm	1							
Ag_ppm	0.27	1						
As_ppm	0.23	0.26	1					
Cu_ppm	0.26	**0.48**	**0.43**	1				
Mo_ Ppm	0.19	0.11	0.08	0.11	1			
Pb_ppm	0.02	0.14	0.18	0.17	0.03	1		
Sb_ppm	0.30	**0.44**	**0.42**	***0.88***	0.21	0.21	1	
Zn_ppm	0.10	0.17	0.22	0.20	0.05	**0.91**	0.24	1

northern segments of the vein. In the central segment ore-shoots are larger and extend up to 50 m.a.s.l; below this elevation they are smaller and irregularly distributed. Towards the southern tip of the vein, ore-shoots occur deeper, whereas in the northern segment they extend from the surface to deep zones, but are smaller and discontinuous (Fig. 8a). High-grade Ag shoots (>25 ppm Ag) reach values up to 750 ppm. Most of the Ag anomalies (Fig. 8b) coincide with Au anomalies. However, the high-grade ore-shoots occur only below the oxidation zone (135 m.a.s.l). High-grade Au and Ag ore-shoots partially overlap with the greatest thicknesses of the vein (>3 m; Fig. 8c), except for isolated patches at greater depths and others in the northern segment that coincide with lower thicknesses (<3 m). Anomalous Cu values are distributed below the oxidation zone, between 135 and 50 m.a.s.l. They occur in ore-shoots with an average grade of 630 ppm, reaching a maximum value of 3 %. In the central segment, there is a main high-grade Cu ore-shoot while in the northern and southern segments high-grade ore-shoots are isolated and small (Fig. 8d). The distribution of Cu is almost identical to that of Ag and Au in the central sector. In the southern segment, high Cu grades overlap high Au values, although the latter are more extensive, and in the northern sector they partially overlap.

Antimony/As values are higher in the central and northern segments of the vein, below the oxidation zone up to 25 m.a.s.l. In the southern sector, zones with high Sb/As values are small, isolated and found in deep levels (up to −50 m.a.s.l) (Fig. 8e). The high Sb/As values coincide with Au anomalies in the southern part of the central segment below the oxidation zone but they partially correlate in the rest of this segment and in the southern and northern segments. In the southern segment Sb/As values correlate strongly with Cu ore-shoots except in the oxidation zone, whereas in the central and northern segments they partially correlate. Sb/As values are low in the shallower levels (except in sectors of the southern segment) and near the intersection with the NE-ENE-striking fault separating the central and northern segments (Fig. 8e). Here, low Sb/As values coincide with high contents of Pb and Zn.

Anomalous Mo contents occur in ore-shoots with an average grade of 440 ppm and can reach very high-grades (up to ±1.5 % Mo). High Mo values occurs between 115 and 0 m.a.s.l in the northern and central segments of the vein and deepen considerably in the southern segment below 100 m.a.s.l. The deepest ore-shoot reaches −70 m.a.s.l. and remains open at depth (Fig. 8f).

Lead and Zn grades show identical distribution along the vein (Fig. 8g, h) and occur in ore-shoots with an average concentration of 3750 and 1980 ppm, respectively and can reach very high-grades up to 11.8 and 6.7 %, respectively. Unlike precious metals, Pb and Zn ore-shoots have a greater areal extension in the central and northern segments of the vein, close to the intersection with the NE-ENE structure where the vein slightly changes its strike to a NW direction (Fig. 2b) and the volcaniclastic units become thicker (north of latitude 4,716,050 mN, Fig. 9a). Unlike any other metal, Pb and Zn high-grades extend up to the end of the northern segment and small Pb ore-shoots crop out in this sector.

Fig. 9 illustrates the host lithologies and the geometry of ore-shoots in relation to the kinematics of the faults that host the Sulfuro Vein in the southern, central and northern segments along the longitudinal section. Ore grade distribution shows a structural compartmentalization controlled by ENE to NE-striking faults.

In the central and southern segments and above 50 m.a.s.l., ore-shoots of Au, Ag and Cu show a gentle plunge of ~10° towards the southern and are associated with greater vein thicknesses. In deeper zones of the southern segment, these ore-shoots show a steep plunge. In the northern segment, north of latitude 4,716,050 mN, ore-shoots show a gentle to moderate plunge (with an average of ~35°) to the south (Fig. 9b - e).

Molybdenum ore-shoots show a sub-horizontal geometry in the central and northern segments, with a gentle plunge of 10° to the south. These ore-shoots exhibits a steep plunge in the southern segment below 100 m.a.s.l. (Fig. 9f). Lead and Zn ore-shoots show a similar geometry characterized by a sub-horizontal attitude with a gentle plunge between 5 and 10° towards the south (Fig. 9g, h). In deep levels of the southern segment, these ore-shoots show a slight increase in plunge (~20° to the south), however never reaching steep values of plunge.

5.3. Metal ratios

At the Sulfuro Vein, the following metal ratios were analyzed: (1) [Au/(Au + Ag)] ∗ 100 to evaluate changes in the fineness of gold (Goodell and Petersen, 1974), (2) [Au/Zn] ∗ 100, [Au/Pb] ∗ 100 and Au/Mo to infer the direction of flow of mineralizing fluids and temperature gradients by contrasting metals that precipitate at low temperatures (Au, Ag) with metals that reflect higher temperatures of deposition (base metals) (Clark and Gemmell, 2018).

Metal ratios are shown in the longitudinal section (Fig. 10a - d). The highest [Au/(Au + Ag)] ∗ 100 values form a sub-horizontal area within and immediately below the supergene alteration zone (Fig. 10a). High [Au/(Au + Ag)] ∗ 100 values are also below 50 m.a.s.l. and par-

a

Factor	Eigenvalues	Variance (%)	Cumulative Variance (%)
1	**2.999**	**37.49%**	**37.49%**
2	**1.654**	**20.68%**	**58.17%**
3	**1.006**	**12.57%**	**70.74%**
4	0.792	9.90%	80.64%
5	0.743	9.29%	89.93%
6	0.604	7.54%	97.48%
7	0.111	1.39%	98.87%
8	0.091	1.13%	100.00%

b

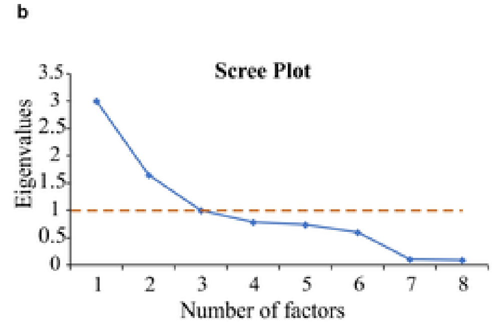

Fig. 6. a Eigenvalues and percentage of variance for the factor analysis applied to the eight chemical elements of the Sulfuro Vein dataset. Extracted components are in bold. **b.** Scree plot of the factor analysis.

Table 2
Factor analysis carried out with 8 analyzed elements (after Varimax rotation).

Element	Factor 1	Factor 2	Factor 3	Communalities
Au_ppm	−0.349	−0.021	**−0.579**	0.458
Ag_ppm	**−0.649**	0.059	−0.140	0.444
As_ppm	**−0.608**	0.156	−0.055	0.397
Cu_ppm	**−0.914**	0.062	−0.051	0.842
Mo_ppm	0.002	0.043	**−0.895**	0.804
Pb_ppm	−0.115	**0.969**	0.011	0.953
Sb_ppm	**−0.879**	0.106	−0.168	0.813
Zn_ppm	−0.153	**0.961**	−0.043	0.949

tially correlate with high Au grades (Fig. 10a). The highest [Au/Zn] ∗ 100, [Au/Pb] ∗ 100 and Au/Mo values are at shallower levels (above ~50 m.a.s.l.) in the central and southern segments of the vein, above ~100 m.a.s.l. in the northern segment, and in sectors below 50 m.a.s.l. along the vein (Fig. 10b - d). The R = (Au ∗ 1000 + Ag ∗ 100)/(Pb + Zn) values illustrated in Fig. 10e are high at shallower levels in the southern and central segments of the vein and in the limit between the northern and central segments, at the intersection with the ENE to NE-striking fault. Localized high values occur in deep levels in the central and southern segments, below 50 and 0 m.a.s.l., respectively.

In some deposits with polymetallic mineralization, the increase in the Pb/Cu ratio away the up-flow zone and the shape of the metal ratio contours are used effectively to infer the direction of movement of the mineralizing solutions (Goodell and Petersen, 1974). This is due to the different solubility between both base metals, since Pb is more soluble and precipitates at lower temperature and further away from the source area than Cu. At the Sulfuro Vein, the Pb/Cu values increases from deep levels in the southern segment to shallower levels to the northern segment (Fig. 10f).

6. Discussion

6.1. Correlations among different metals distribution and the ore minerals

Statistical exploration methods applied to the geochemical data population represent the main metallogenetic elements associations and are consistent with the mineralogy described in the mineralizing pulses that fill the Sulfuro Vein. Factor 1 represents the metallogenetic elements association of the stage 8, dominant in the southern and central sectors of the vein during the episode E2 (Fig. 5b). The moderate positive correlation between Cu, Sb and Ag and the high positive correlation between the first two are in accord with the presence of tetrahedrite, while the moderate positive correlation of As with Cu and Sb coincides with the presence of tennantite in the stage 8. Moreover, the moderate positive correlation of Ag with Sb and the low correlation with As, would be due to the fact that Ag is generally higher in the tetrahedrite subgroup (Mason, n.d; unpublished results). Factor 2 and the high positive correlation between Pb and Zn represent the association of galena with sphalerite in the stage 8 during episode E2 in the northern segment of the vein (Fig. 5c, d). Factor 3 represents the main metallogenetic elements association, Mo and Au, of the stage 3 during E1 (Fig. 4f - h). The slightly higher correlation of Au with Ag, As, Cu, Mo and Sb could be due to the fact that the episodes enriched in Au precipitated molybdenite and chalcopyrite with tennantite-tetrahedrite (Figs. 4e - i, 5b, f).

The high contents of the analyzed elements (Au, Ag, Cu, Mo, Pb, Zn and Sb) between depths of 50 and 100 m.a.s.l. (Fig. 8) could be attributed to the opening of the structure and rapid pressure release followed by boiling or flashing of the hydrothermal fluids. Boiling is evidenced by the presence of rhombic adularia in the deeper parts of the vein (Fig. 4a; Browne and Ellis, 1970; Browne, 1978; Henley, 1985; Hedenquist, 1990) and also lead to silica supersaturation, which results in the for-

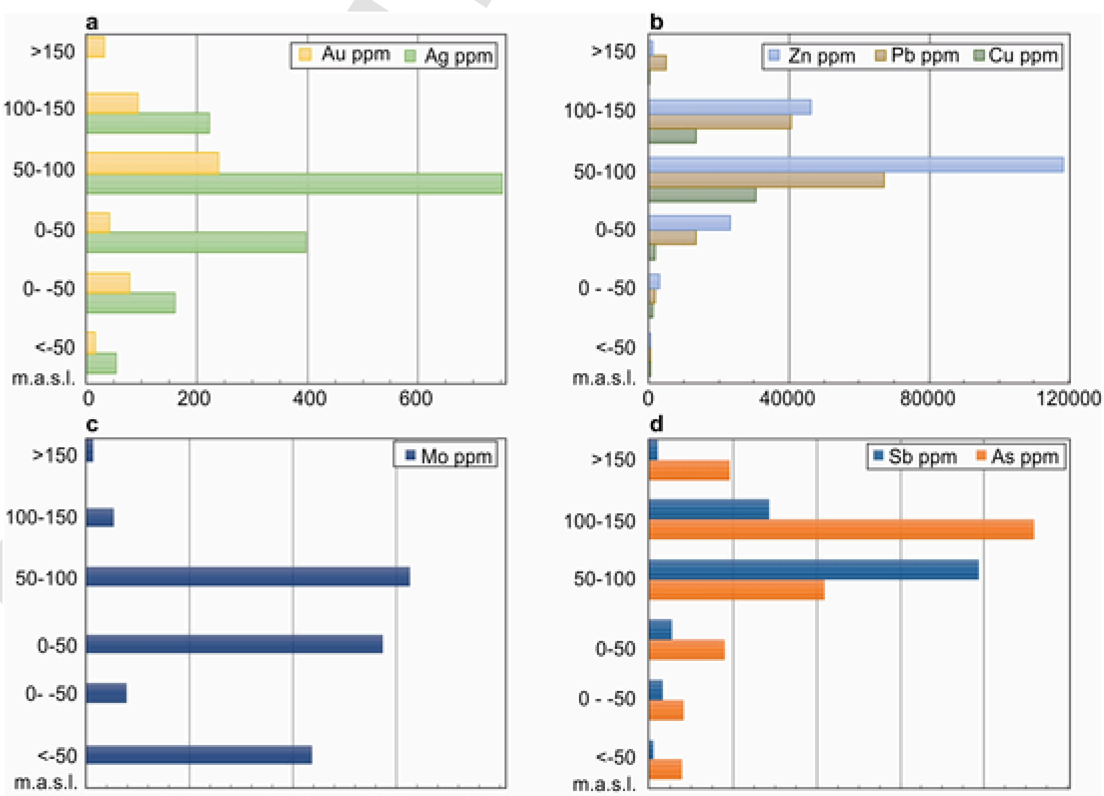

Fig. 7. Variation of metals content as a function of depth in the Sulfuro Vein. **a** Gold and Ag. **b** Zinc, Pb and Cu. **c** Molybdenum. **d** Antimony and As. (For interpretation of the references to colour in this figure the reader is referred to the web version of this article.) (For interpretation of the references to colour in this figure legend, the reader is referred to the web version of this article.)

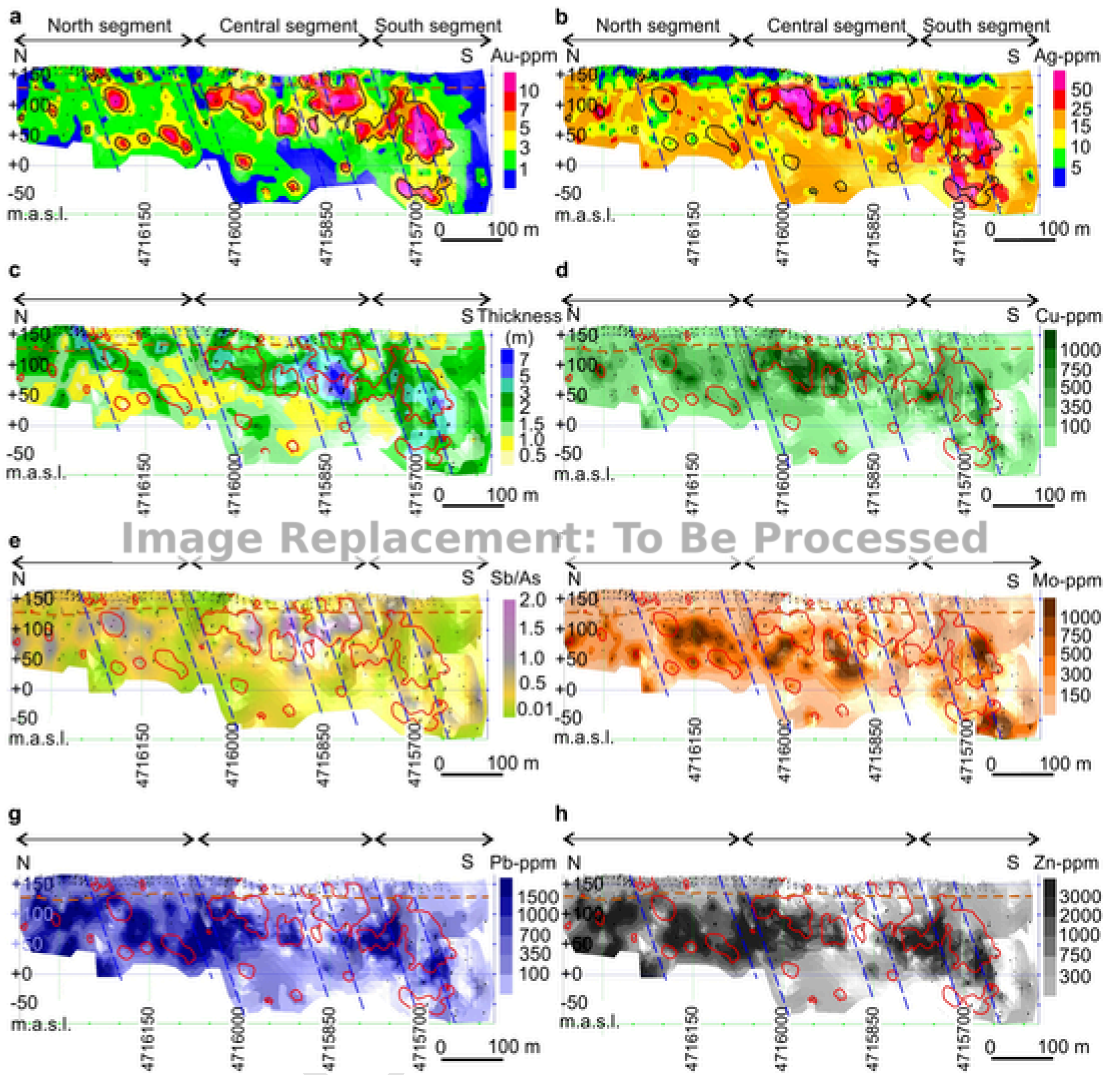

Fig. 8. Ore grade distribution in the longitudinal section of the Sulfide vein. **a** Gold distribution. **b** Silver distribution. **c** Variation of vein thickness in meters. **d** Copper distribution. **e** Sb/As ratio. **f** Molybdenum distribution. **g** Lead distribution. **h** Zinc distribution. Faults are indicated in blue dashed lines, the base of the supergene alteration is indicated with a brown dashed line. Contours in black (a, b) and red (rest of the diagrams) indicate Au anomalies >5 g/t Au. Black dot points represent the position of composites used for modeling. (For interpretation of the references to colour in this figure the reader is referred to the web version of this article.) (For interpretation of the references to colour in this figure legend, the reader is referred to the web version of this article.)

mation of the described quartz textures (e.g. colloform banded and microcrystalline mosaic textures as shown in Fig. 4d, k; Fournier, 1985; Dong et al., 1995; Moncada et al., 2012; Shimizu, 2014). These processes could lead to the formation of the breccias (Simmons et al., 2005) cemented by base metal sulfides with Au and Ag during the episode E2 (Fig. 4d). The metals analyzed decrease towards the surface and with depth, except for As that shows higher concentrations at shallow levels (between 100 and 150 m.a.s.l.) and Mo that, although it decreases towards the surface, it shows high contents at depth. The presence of this metal in the deepest levels of the vein is possibly due to its precipitation from a hydrothermal fluid at the beginning of the vein formation (episode E1) under physico-chemical conditions different from episode E2.

When comparing the distribution of Au, Ag and Cu with Mo, Pb and Zn (Fig. 8), it is observed that ore-shoots of the first three metals exhibit a greater distribution in the southern and central segments of the vein, while ore-shoots of Mo, Pb and Zn occur along the entire longitudinal section. However, high Mo contents decrease from the latitude 4,716,200 mN to the north and high Pb and Zn values continue in this direction. These differences in metal concentrations and distribution along the vein segments can be interpreted as the effect of different concentrations and solubility of these metals in the mineralizing fluids (Fontboté et al., 2017) during the deposition of the E2 episode, in which Pb and Zn would have precipitated with Cu, Au, Ag and Sb in the southern and central segments, and continued precipitating at lower temperature (Fontboté et al., 2017) in the north sector, where the fluid was exhausted in Cu, Au, Ag and Sb. Molybdenum shoots also have a broad distribution in the central and northern segments of the vein, but Mo shows low correlation with Pb and Zn given that it precipitated in a previous mineralizing episode (E1). The broad distribution of Mo, except in deeper part of the vein, could reflect its remobilization by hydrothermal fluids during episode E2 (Fig. 4d). In addition, high Mo, Pb and Zn ore-shoots partially overlap the Au-rich zones and have greater extension at slightly greater depths. Gold shows similar distribution to Ag throughout the vein section, and to Cu in the central and southern segments, although in the latter Cu ore-shoots have less areal extension (Fig. 8d). Unlike Cu and Ag, Au shows high concentrations in the supergene zone. It is interpreted that this behaviour could be due to the dissolution of sulfides and sulfosalts during the supergene alteration and release of Au incorporated as micro (Figs. 4f, h; 5b, f, g) or nanoparticles in these minerals and to the high mobility of Ag and Cu with respect to Au (Reich and Vasconcelos, 2015). Lead also seems to be less

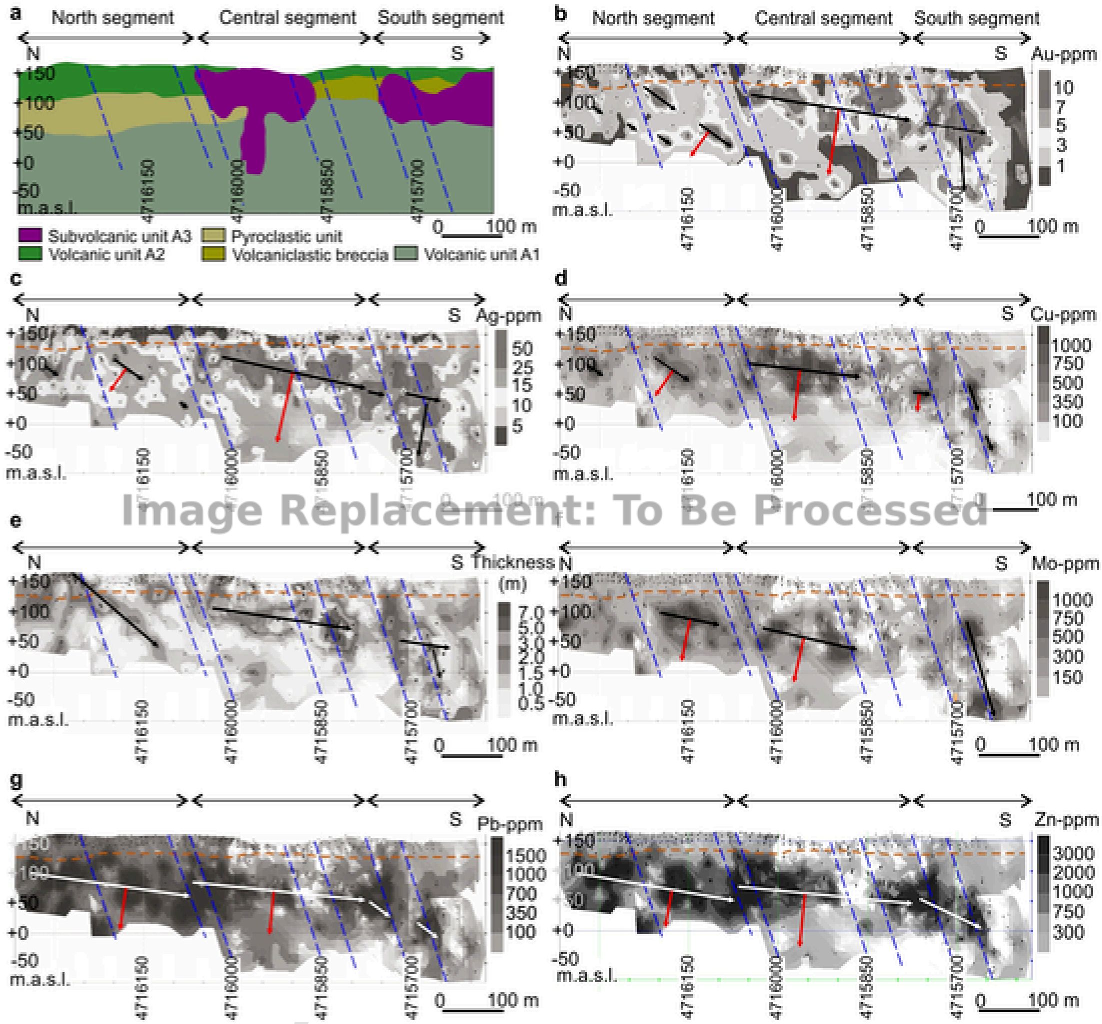

Fig. 9. Host lithologies and ore-shoots geometry along the longitudinal section of the Sulfuro Vein. Black arrows (white in the case of 9 g and 9 h) represent the position and extent of the anomalous contents (ore-shoots) for each element (see text for details). Red arrows show movement direction of the hanging-wall block. **a** Host lithologies. **b** Gold ore-shoots. **c** Silver ore-shoots. **d** Copper ore-shoots. **e** Vein thickness. Black arrows show the main sub-horizontal ore-shoot in the central segment, the steeply plunging ore-shoot in the southern segment, and the gently to moderately plunging ore-shoot in the northern segment. **f** Molybdenum ore-shoots. **g** Lead ore-shoots. **h** Zinc ore-shoots. (For interpretation of the references to colour in this figure the reader is referred to the web version of this article.) (For interpretation of the references to colour in this figure legend, the reader is referred to the web version of this article.)

affected by the supergene alteration in the northern segment, which is consistent with the geochemical behaviour of this immobile element in the supergene environment (Thornber, 1985).

The relationships between precious and base metals indicate that the latter, which are less soluble and precipitate from fluids at higher temperatures (Buchanan, 1981; Hedenquist et al., 2000; Simmons et al., 2005), are concentrated in the deeper parts of the vein; the exception is represented by Zn and Pb which are also found at shallow levels in the northern segment since these elements can remain in solution and precipitate at lower temperatures (Hemley et al., 1992; Fontboté et al., 2017)). The paleo-direction of the fluid-flow given by the ratios $R = (Au * 1000 + Ag * 100)/Pb + Zn$ and P/Cu (Fig. 10e, f) suggests that the mineralizing hydrothermal fluids flowed from the deepest zones of the southern segment to the north.

6.2. *Structural and lithological controls on ore distribution*

Ore-shoots consist of sectors of high metal content, and represent zones of maximum paleo-permeability along faults developed prior or concomitant to mineralization and that are perpendicular to the fault displacement vector (Nelson, 2006). Ore-shoots present a diversity of forms, which reflect the influence of structural and lithological controls (Simmons et al., 2005). At the deposit scale, the intersection between faults and competence contrasts between different host rocks, and/or permeability anisotropy can influence direction of flow of hydrothermal fluids and the morphologies of ore shoots (Cox, 2005).

The ore-shoots at the Sulfuro Vein are characterized by complex hydrothermal breccia textures that suggest repeated events of fracturing, pressure release, and subsequent infill during vein formation (Fig. 4c, d). Various investigations have shown that fault and/or fracture systems in hydrothermal systems with strong structural control are rapidly cemented and suggest that repeated displacement events are necessary for the multiple opening and filling events during vein formation (Cox et al., 2001; Cox, 2005; Simmons et al., 2005; Micklethwaite, 2009). This repetition of events can be caused by fluid pressure or may occur in response to regional and/or local stresses (Micklethwaite, 2009). Further structural investigations have also recognized the important role of seismicity in increasing permeability and consequent formation of mineral deposits (Sibson, 1987, 1996; Micklethwaite and Cox, 2004; Woodcock et al., 2007).

Fernández et al. (2020) highlighted the importance of inherited structures in the development of epithermal deposits of economic interest at the La Paloma district. The reactivation of pre-existing joints as hybrid extensional-shear fractures generated different geometries of

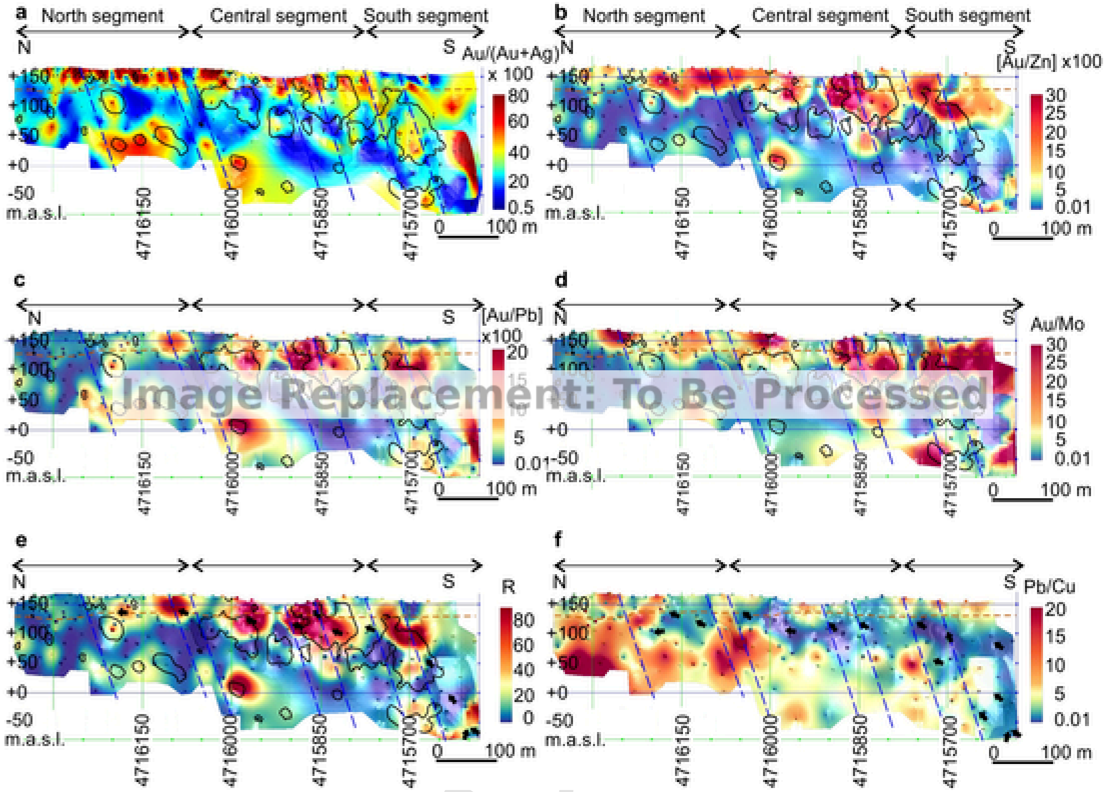

Fig. 10. Metal ratios along the longitudinal section of the Sulfuro Vein. **a** Au/(Au + Ag) × 100. **b** [Au/Zn] × 100. **c** [Au/Pb] × 100. **d** Au/Mo. **e** R = (Au ∗ 1000 + Ag ∗ 100)/Pb + Zn. **f** Pb/Cu. Contours in black (a, b) and red (rest of the diagrams) indicate Au anomalies >5 g/t Au. Black arrows indicate paleo-direction movement of the mineralizing hydrothermal fluids. (For interpretation of the references to colour in this figure the reader is referred to the web version of this article.) (For interpretation of the references to colour in this figure legend, the reader is referred to the web version of this article.)

the ore-shoots. These shoots range from horizontal/sub-horizontal to vertical for displacements with a dominant normal and strike-slip component, respectively (Nelson, 2006). Since ore-shoots tend to be parallel to the intermediate stress direction (σ2) (Nelson, 2006), the multiple permutations between σ_2 and σ_3 associated with the formation of the Sulfuro and further veins in the La Paloma region (Fernández et al., 2020) make the system even more complex. However, this complexity is not the result of different deformation events in response to important changes in the regional stress field and/or in the tectonic environment. Rather, the complex distribution of the ore shoots is the result of the reactivation of a network of pre-existing joints with various orientations within the framework of a stress field dominated by a vertical σ_1 and multiple permutations between the σ_2 and σ_3 principal stress axes (Fernández et al., 2020).

The sub-horizontal geometry of the thickest areas of the Sulfuro Vein and of the ore-shoots is consistent with dominant extensional faulting during mineralization. The ore-shoots steepen to the south, where some of them (Au, Ag, Cu and Mo) become steeply plunging to vertical (Fig. 9b - d, f). This feature suggests a significant strike-slip component of motion along the southern vein segment during ore deposition and/or vertical fluid flow enhanced by the intersection of the Sulfuro vein with ENE- and N-striking faults (Fig. 2b). In any case, the southern vein segment could represent the upward fluid flow zone of hydrothermal system (4,715,700 in Fig. 9). The intensity of the argillic alteration and silicification identified in the southeastern sector of the district during field mapping and ASTER image processing (Telluris Consulting, 2011; unpublished results), also suggests a large flow of hydrothermal fluids in this sector. This inference is consistent with the metal zonation and the relationships between precious and base metals (Figs. 8, 10), which also indicate a S—N thermal gradient and ore-fluids sourced from the southern termination of the vein.

Some of the NE to ENE-striking faults could have remained active after the precipitation of the metals since the ore-shoots show segmentation controlled by these faults (Fernández et al., 2020). In addition, there is evidence of stratigraphic separation of approximately 25 m generated by these structures.

Northward, where the structure has a subtle NW strike swing (4,716,050 in Fig. 2b), Au, Ag and Cu ore-shoots are smaller and irregularly distributed (Fig. 8a, b, d). Gold, Ag and Cu ore-shoots and the thickest areas show gentle to moderate plunges (dominantly around 35° towards the south; Fig. 9b - e). Given that the strike-slip component associated with these hybrid extension-shear fractures depends on the obliquity of the structure with respect to the maximum stretching direction (which in this case is ENE oriented, as indicated by the analysis of fault-slip data carried out by Fernández et al., 2020) it is likely that kinematics with larger strike-slip components along the NW-striking vein segment in the northern sector favoured dilation and fluid flow. However, this strike-slip component played a less important role during Zn and Pb precipitation, as explained in the following. In the vicinity of latitude 4,716,050 mN, which marks the boundary between the central and northern segments of the vein, the largest Zn and Pb ore-shoots that extend northward are located (Fig. 8g, h). In this sector, volcaniclastic rocks form continuous and thick deposits intercalated within the coherent andesites (Figs. 2a; 9a). Zinc and Pb mineralizations are disseminated in the volcaniclastic rocks and in veins up to 1 cm thick (Fig. 5d, e). Therefore, it may be envisaged that the size of the ore-shoots in this sector are controlled, in addition to metal concentrations and solubility in the mineralizing fluids as explained in Section 6.1, by the porosity of the volcaniclastic host rocks that favoured the percolation of hydrothermal fluids and the formation of more extensive mineralized bodies, rather than the structural control exerted by fault kinematics.

7. Conclusive remarks

The epithermal Au—Ag (Zn, Pb, Mo and Cu) Sulfuro Vein occupies NNW to NW-striking hybrid extension-shear fractures (with variable strike-slip components of motion) hosted in the Middle Jurassic andesitic volcanic rocks (Bajo Pobre Formation). Geochemical analyses of this vein, the most important in the La Paloma district, provide new insights into the controls exerted by lithological and structural features, besides fluid chemistry and metal remobilization, in the formation of ore-shoots. Vein thickness and ore contents displayed on top of 2D, as well as along-strike representations of the analyzed structure furnish a comprehensive picture of the 3D architecture of the ore body. Furthermore, the reconstruction of subsequent mineralization episodes allows obtain information on the progression of the mineralization process through time. The main insights into such a 4D understanding of ore-shoot formation are summarized in the points below.

(1) Correlation coefficients between metals and elements associations obtained from factor analysis are consistent with the ore mineralogy described in the main mineralizing stages 3 and 8 of episodes E1 and E2, respectively, that characterize the ore shoots.
(2) The highest values of Au, Ag, Cu, Mo, Pb, Zn and Sb are concentrated at depths between 50 and 100 m.a.s.l., while high Mo values are recorded also at greater depths (−50 m.a.s.l.) in the southern segment.
(3) Metal distribution along the Sulfuro Vein is consistent with the paragenetic sequence. The Au-bearing molybdenite-rich band with subordinated amounts of chalcopyrite and tennantite-tetrahedrite precipitated at the beginning of the vein infill during episode E1 and was brecciated and remobilized by later stages of vein infill.
(4) During episode E2, Au precipitated as micro-inclusion within pyrite and chalcopyrite and interstitial between pyrite crystal during the main mineralization stages. These were followed by galena containing minor Au micro-inclusion and sphalerite, which continued precipitating at lower temperatures in the northern sector of the vein, where the fluid was exhausted in Cu, Au, Ag.
(5) The sub-horizontal geometry of the ore shoots and the areas of greater thickness suggest dominant extensional kinematics, except in the northern segment where Au, Ag and Cu shoots and the areas of greater thickness reflect a larger strike-slip component of motion. On the other hand, the latter strike-slip component seems not to have exerted an important control in the distribution of Zn and Pb in this sector, where the porosity of volcaniclastic rocks played a major role in the formation of more extensive Zn and Pb ore-shoots.
(6) The geochemical distribution of metals shows a slight vertical zonation and a distinct lateral zonation, which suggests that hydrothermal fluids flowed from deep zones in the southern segment of the vein to the north through the NNW-striking fractures. Steepening and deepening of the ore-shoots towards the south reaffirms the previous conclusion.

Supplementary data to this article can be found online at https://doi.org/10.1016/j.gexplo.2022.107053.

CRediT authorship contribution statement

María Lis Fernández : Conceptualization, Methodology, Formal analysis, Investigation, Writing – original draft, Writing – review & editing, Visualization. **Marta Franchini :** Conceptualization, Methodology, Formal analysis, Investigation, Writing – original draft, Writing – review & editing, Visualization, Funding acquisition. **Stefano Mazzoli :** Formal analysis, Investigation, Writing – review & editing. **Pablo J. Caffe :** Formal analysis, Investigation, Writing – review & editing. **Alejandro Garrone :** Methodology, Software.

Declaration of competing interest

The authors declare that they have no known competing financial interests or personal relationships that could have appeared to influence the work reported in this paper.

Acknowledgments

This research represents part of the first author's PhD thesis in preparation at the Universidad Nacional del Comahue and Universidad Nacional de Río Negro. The study was supported CONICET (PIP 105); FONCyT (PICT-2017-4577); Universidad Nacional del Comahue (PIP 04/I250). We express our appreciation to the Exploration Manager, Lic. Silvio Franco, and to the exploration staff of ex Minera Don Nicolas S.A. mining company for allowing access to subsurface information and samples. The authors are very grateful to Dr. David Lentz for his collaboration in obtaining micro-XRF EDS geochemical maps and to Dr. Ramón Aguirre Maturana and Dra. Elda Beatriz Micheli for their valuable comments and explanations on the statistical analysis techniques.

References

Archangelsky, S., 1967. Estudio de la Formación Baqueró, Cretácico inferior de Santa Cruz, Argentina. Rev. Museo Plata, Paleontol. 5, 63–171.
Archangelsky, S., Cuneo, R., 1984. Zonación del Pérmico continental Argentino sobre la base de sus plantas fósiles. In: 3° Congreso Latinoamericano de Paleontología. pp. 143–153.
Arribas, A., Schalamuk, I.B., de Barrio, R.E., Fernández, R.R., 1996. Edades radiometricas de mineralizaciones auriferas del Macizo del Deseado, Provincia de Santa Cruz, Argentina. In: XXIX Congresso Brasileiro de Geología, 7, pp. 254–257.
Arrondo, O., 1972. Estudio geológico y paleontológico de la zona de la Estancia La Juanita y alrededores, provincia de Santa Cruz, Argentina. Rev. Museo Plata, Paleontol. 7, 1–194.
Bluman, A.G., 2003. Elementary Statistics, A Step by Step Approach. second ed. Mc Graw-Hill, New York. 637 pp.
Browne, P.R.L., 1978. Hydrothermal alteration in active geothermal fields. Annu. Rev. Earth Planet. Sci. 6, 229–250.
Browne, P.R.L., Ellis, A.J., 1970. The Ohaki-Broadlands hydrothermal area, New Zealand; mineralogy and related geochemistry. Am. J. Sci. 269 (2), 97–131.
Buchanan, L.J., 1981. Precious-metal deposits associated with volcanic environments in the Southwest. In: Dickinson, W.R., Payne, W.D. (Eds.), Relations of Tectonics to Ore Deposits in the Southern Cordillera. Arizona Geological Society Digest, 14, pp. 237–262.
Clark, L.V., Gemmell, J.B., 2018. Vein stratigraphy, mineralogy, and metal zonation of the kencana low-sulfidation epithermal Au-Ag deposit, Gosowong goldfield, Halmahera Island, Indonesia. Econ. Geol. 113, 209–236.
Cox, S.F., 2005. Coupling between deformation, fluid pressures, and fluid flow in ore producing hydrothermal systems al depth in the crust. In: Economic Geology 100th Anniversary. pp. 39–75.
Cox, S.F., Knackstedt, M.A., Braun, J., 2001. Principles of structural control on permeability and fluid flow in hydrothermal systems. In: Richards, J.P., Tosdal, R.M. (Eds.), Structural Controls on Ore Genesis. Reviews in Economic Geology, 14, pp. 1–24.
Davis, J.C., 2002. Statistics and Data Analysis in Geology. third ed. Wiley, New York. 638 pp.
Di Persia, C., 1962. Acerca del descubrimiento del Precámbrico en la Patagonia Extrandina (provincia de Santa Cruz). In: Primeras Jornadas Geológicas Argentinas, Buenos Aires, Actas, 2, pp. 65–68.
Dietrich, A., Gutiérrez, R., Nelson, E., Laye, P., 2012. Geology of the Huevos Verdes vein system and San José district, Deseado massif, Patagonia, Argentina. Mineral. Deposita 47, 233–249. https://doi.org/10.1007/s00126-010-0327-2.
Dong, G.Y., Morrison, G., Jaireth, S., 1995. Quartz textures in epithermal veins, Queensland—classification, origin, and implication. Econ. Geol. 90, 1841–1856.
Dubé, B., Zubia, M., Dunning, G., Villeneuve, M., 2000. Estudio geocronológico de los campos filoneanos de baja sulfuración hospedados en la formación Chon Aike en el Macizo del Deseado, Provincia de Santa Cruz. In: Zubia, M., Genini, A. (Eds.), Yacimientos auroargentíferos epitermales del Macizo del Deseado, Provincia de Santa Cruz. SEGEMAR Serie Contribuciones Técnicas Recursos Minerales, 13, pp. 11–17.
Echavarría, L.E., Schalamuk, I.B., Etcheverry, R.O., 2005. Geologic and tectonic setting of Deseado Massif epithermal deposits, Argentina, based on El Dorado-Monserrat. J. S. Am. Earth Sci. 19 (4), 415–432.

Fernández, M.L., Mazzoli, S., Zatti, M., Savignano, E., Genge, M.C., Garrone, A., Franchini, M., 2020. Structural controls on Jurassic gold mineralization, and Cretaceous-Tertiary exhumation in the foreland of the southern Patagonian Andes: new constraints from La Paloma area, Deseado Massif, Argentina. Tectonophysics 775, 228–302.

Fernández, R.R., Blesa, A., Moreira, P., Echeveste, H., Mykietiuk, K., Andrada De Palomera, P., Tessone, M., 2008. Los depósitos de oro y plata vinculados al magmatismo Jurásico de la Patagonia: Revisión y perspectivas Para la exploración. Rev. Asoc. Geol. Argent. 63 (4), 665–681.

Folguera, A., Fernandez Paz, L., Iannelli, S., Navarrete, C., Echaurren, A., Gianni, G., Butler, K.L., Borton, B.K., Litvak, V., Encinas, A., Orts, D., 2020. The origin of the san Jorge gulf basin in the context of the mesozoic-cenozoic evolution of Patagonia. J. S. Am. Earth Sci. 97, 102–422.

Fontboté, L., Kouzmanov, K., Chiaradia, M., Pokrovski, G.S., 2017. Sulfide minerals in hydrothermal deposits. Elements 13, 97–103. https://doi.org/10.2113/gselements.13.2.97.

Fournier, R.O., 1985. The behavior of silica in hydrothermal solutions. In: Berger, B.R., Bethke, P.M. (Eds.), Geology and Geochemistry of Epithermal Systems, 2. Reviews in Economic Geology, 2, pp. 45–60.

Garrone, n.d., A. Garrone , Unpublished results. Reporte de Recursos – Sistema Sulfuro. Internal Report by Minera Don Nicolás S.A.

Giacosa, R., Zubia, M., Sánchez, M., Allard, J., 2010. Meso-Cenozoic tectonics of the southern Patagonian foreland: structural evolution and implications for Au–Ag veins in the eastern Deseado Region. J. S. Am. Earth Sci. 30, 134–150.

Goodell, P.C., Petersen, U., 1974. Julcani mining district, Peru: a study of metal ratios. Econ. Geol. 69, 347–361.

Gorring, M., Kay, S., Zeitler, P., Ramos, V., Rubiolo, D., Fernández, M., Panza, J., 1997. Neogene Patagonian plateau lavas. Continental magmas associated with ridge collision at the Chile triple junction. Tectonics 16 (1), 1–17.

Guido, D., Schalamuk, I., 2003. Genesis and exploration potential of epithermal deposits from the Deseado Massif, Argentinean Patagonia. In: Eliopoulos, D. (Ed.), Mineral Exploration and Sustainable Development. Society for Geology Applied to Mineral Deposits. Balkema-Rotterdam, Athens, Greece, pp. 493–496.

Guido, D., Escayola, M.P., Schalamuk, I., 2004. The basement of the Deseado Massif at Bahía Laura, Patagonia, Argentina: a proposal for its evolution. J. S. Am. Earth Sci. 16, 567–577.

Guido, D., Escayola, M., de Barrio, R., Schalamuk, I., Franz, G., 2006. La Formación Bajo Pobre (Jurásico) en el este del Macizo del Deseado, Patagonia Argentina: Vinculación con el Grupo Bahía Laura. Rev. Asoc. Geol. Argent. 61 (2), 187–196.

Guido, D.M., 2004. Subdivisión litofacial e interpretación del volcanismo jurásico (Grupo Bahía Laura) en el este del Macizo del Deseado, provincia de Santa Cruz. Rev. Asoc. Geol. Argent. 59 (4), 727–742.

Guido, D.M., Campbell, K.A., 2011. Jurassic hot spring deposits of the Deseado Massif (Patagonia, Argentina): characteristics and controls on regional distribution. J. Volcanol. Geotherm. Res. 203, 35–47.

Guido, D.M., Jovic, S.M., 2019. Relevance of epithermal deposits in Argentina. available at. In: South American Metallogeny: Sierra to Craton. Society of Economic Geologist Conference, Santiago, Chile. Conference Proceedings. www.segwerb.org.

Guido, D.M., Jovic, S.M., Schalamuk, I.B., 2005. A new metallogenic association (Sn–Cd–In–Zn–Ag–Au) in the Deseado Auroargentiferous province, Deseado Massif, Patagonia, Argentina. Meeting the Global Challenge — 8th SGA Meeting, Beijing, China. Miner. Deposit Res. 2, 965–968.

Hair, J.F., Black, W.C., Babin, B.J., Anderson, R.E., 2010. Multivariate Data Analysis. 7th ed. Prentice Hall, New Jersey. 786 pp.

Hechem, J., Homovc, J.F., 1988. Facies y paleoambientes volcaniclásticos en el Nesocratón del Deseado. Bol. Inf. Petroleras 16, 2–23.

Hedenquist, J.W., 1990. The thermal and geochemical structure of The Broadlands-Ohaaki geothermal system, New Zealand. Geothermics 19 (2), 151–185.

Hedenquist, J.W., Arribas, A., Gonzalez-Urien, E., 2000. Exploration for epithermal gold deposits. Rev. Econ. Geol. 13, 221–244.

Hemley, J.J., Cygan, G.L., Fein, J.B., Robinson, G.R., D'Angelo, W.M., 1992. Hydrothermal ore-forming processes in the light of studies in rock-buffered systems: II. Some general geologic applications. Econ. Geol. 87, 23–43.

Henley, R.W., 1985. The geothermal framework of epithermal deposits. In: Berger, B.R., Bethke, P.M. (Eds.), mal deposits. In: B.R.BergerP.M.Bethke (Eds.), Geology and Geochemistry of Epithermal Systems. Reviews in Economic Geology, 2, pp. 1–24. https://doi.org/10.2113/gsecongeo.59.4.538.

Howarth, R.J., Sinding-Larsen, R., 1983. Multivariate analysis. In: Govett, G.J.S. (Ed.), Handbook of Exploration Geochemistry. Statistics and data analysis in geochemical prospecting, Amsterdam, vol. 2. 437 pp.

Jovic, S., Guido, D., Schalamuk, I., Ríos, F., Tassinari, C., Recio, C., 2011. Pingüino in-bearing polymetallic vein deposit, Deseado Massif, Argentina: characteristics of mineralization and ore-forming fluids. Mineral. Deposita 46, 257–271.

Kaiser, H.F., 1958. The Varimax criterion for analytic rotation in factor analysis. Psychometrika 23, 187–200.

López, L., Jovic, S.M., Guido, D.M., Permuy Vidal, C., Páez, G.N., Ruiz, R., 2015. Geochemical distribution and supergene behavior of indium at the Pingüino epithermal polymetallic vein system, Patagonia, Argentina. Ore Geol. Rev. 64, 747–755.

Telluris Condulting Ltd, n.d., Telluris Condulting Ltd ., Unpublished results. Structural Study of the Don Nicolas and Chispas Districts, Santa Cruz, Argentina. Internal Report by Minera IRL Limited.

Mason, n.d., D.R. Mason , Unpublished results. Petrographic Descriptions for Forty-eight Rock Samples from Martinetas and La Paloma Prospects at the Don Nicolas Au-Ag Epithermal Deposit, Santa Cruz Province, Argentina. Internal Report by Minera IRL Limited.

Micklethwaite, S., 2009. Mechanisms of faulting and permeability enhancement during epithermal mineralisation: Cracow goldfield, Australia. J. Struct. Geol. 31, 288–300.

Micklethwaite, S., Cox, S.F., 2004. Fault-segment rupture, aftershock-zone fluid flow, and mineralization. Geology 32, 813–816.

Moncada, D., Mutchler, S., Nieto, A., Reynolds, T.J., Rimstidt, J.D., Bodnar, R.J., 2012. Mineral textures and fluid inclusion petrography of the epitermal Ag-Au deposits at Guanajuato, Mexico: application to exploration. J. Geochem. Explor. 114, 20–35.

Moore, D.M., Reynolds, Jr, R.C., 1997. X-Ray diffraction and the identification and analysis of clay minerals. Oxford University Press, New York, p. 378.

Mugas Lobos, A.C., Márquez-Zavalía, M.F., Lira, R., Hernández, L.B., 2021. Mineralogy and microthermometry of the Escondida, Gabriela and Margarita mineralized structures from the Cerro Moro epithermal deposit, Deseado Massif, Argentina. J. S. Am. Earth Sci. 105. https://doi.org/10.1016/j.jsames.2020.103077.

Navarrete, C., Gianni, G., Encinas, A., M´arquez, M., Kamerbeek, Y., Valle, M., Folguera, A., 2019. Triassic to Middle Jurassic geodynamic evolution of southwestern Gondwana: from a large flat-slab to mantle plume suction in a rollback subduction setting. Earth Sci. Rev. 194, 125–159.

Nelson, E.P., 2006. Drill-hole design for dilational ore shoot targets in fault-fill veins. Econ. Geol. 101, 1079–1085.

Páez, G.N., Ruiz, R., Guido, D.M., Ríos, F.J., Subias, I., Recio, C., Schalamuk, I.B., 2016. Highgrade ore shoots at the Martha epithermal vein system, Deseado Massif, Argentina: the interplay of tectonic, hydrothermal and supergene processes in ore genesis. Ore Geol. Rev. 72, 546–561.

Paine, M., 1998. Manual on Statistical Analysis of Environmental Data. Vol II. CANMET/MMSL–INTEMIN. 259 pp.

Godoy Prietoand Palluzi, n.d., D. Godoy Prieto A. Palluzi , Unpublished results. Estratigrafía de la Veta Sulfuro, Prospecto La Paloma. Internal Report by Minera Don Nicolás S.A.

Pankhurst, R.J., Leat, P.T., Sruoga, P., Rapela, C.W., Márquez, M., Storey, B.C., Rilley, T.R., 1998. The Chon Aike province of Patagonia and related rocks in West Antarctica: a silicic large igneous province. J. Volcanol. Geotherm. Res. 81, 113–136.

Pankhurst, R.J., Riley, T.R., Fanning, C.M., Kelley, S.P., 2000. Episodic silicic volcanism in Patagonia and the Antarctic Peninsula: chronology of magmatism associated with the break-up of Gondwana. J. Petrol. 41 (5), 605–625.

Panza, J., Franchi, M., 2002. Magmatismo Basáltico Cenozoico Extraandino. In: Haller, M.J. (Ed.), Geología y Recursos Naturales de Santa Cruz. 15° Congreso Geológico Argentino, Buenos Aires. pp. 259–284.

Permuy Vidal, C., Guido, D.M., Jovic, S.M., Bodnar, R.J., Moncada, D., Melgarejo, J.C., Hames, W., 2016. The Marianas-San Marcos vein system: characteristics of a shallow low sulfidation epithermal Au–Ag deposit in the Cerro Negro district, Deseado Massif, Patagonia, Argentina. Mineral. Deposita 51 (6), 725–748.

Ramos, V.A., 2002. Evolución Tectónica. In: Haller, M.J. (Ed.), Recursos Naturales de Santa Cruz, Relatorio XV Congreso Geológico Argentino. Asociación Geológica Argentina, Buenos Aires, pp. 365–387.

Rapela, C.W., Pankhurst, R.J., 1996. Monzonite suites: the innermost Cordilleran plutonism of Patagonia. Trans. R. Soc. Edinb. Earth Sci. 87, 193–203.

Rapela, C.W., Pankhurst, R.J., Fanning, C.M., Hervé, F., 2005. Pacific subduction coeval with the Karoo mantle plume: the early Jurassic Subcordilleran belt of northwestern Patagonia. Geol. Soc. Lond. Spec. Publ. 246, 217–239.

Reich, M., Vasconcelos, P.M., 2015. Geological and Economic significance of Supergene Metal Deposits. Elements 11 (5), 305–310. https://doi.org/10.2113/gselements.11.5.305.

Riley, T.R., Leat, P.T., Pankhurst, R.J., Harris, C., 2001. Origins of large volume rhyolitic volcanism in the Antarctic Peninsula and Patagonia by crustal melting. J. Petrol. 42, 1043–1065.

Schalamuk, I., de Barrio, R., Zubia, M., Genini, A., Echeveste, H., 1999. Provincia Auroargentífera del Deseado, Santa Cruz. In: Zappettini, E. (Ed.), Recursos Minerales de la República Argentina. Instituto de Geología y Recursos Minerales SEGEMAR, pp. 1177–1188.

Schalamuk, I.B., Zubia, M., Genini, A., Fernández, R.R., 1997. Jurassic epithermal Au–Ag deposits of Patagonia, Argentina. Ore Geol. Rev. 12 (3), 173–186.

Secretaría de Minería Argentina, 2022. Centro de Información Abierta a la comunidad sobre la Actividad Minera en Argentina (SIACAM). https://www.argentina.gob.ar/produccion/mineria/siacam.

Shimizu, T., 2014. Reinterpretation of quartz textures in terms of hydrothermal fluid evolution at the Koryu Au-Ag deposit, Japan. Econ. Geol. 109, 2051–2065.

Sibson, R.H., 1987. Earthquake rupturing as a mineralizing agent in hydrothermal systems. Geology 15, 701–704.

Sibson, R.H., 1996. Structural permeability of fluid-driven fault-fracture meshes. J. Struct. Geol. 18, 1031–1042.

Simmons, S.F., White, N.C., John, D.A., 2005. In: Geological Characteristics of Epithermal Precious and Base Metal Deposits. Economic Geology 100th Anniversary. pp. 485–522.

Squire, R.J., Robinson, J.A., Rawling, J.T., Wilson, C.J.L., 2008. Controls on ore shoot locations and geometries at the stawell gold mine, Southeastern Australia: contributions of the volcanosedimentary, alteration, and structural architecture. Econ. Geol. 103, 1029–1041.

Sruoga, P., Busteros, A., Giacosa, R., Kleiman, L., Japas, S., Maloberti, A., Martínez, H., 2008. Análisis litofacial y estructural del Complejo Bahía Laura en el área El Dorado - Monserrat, provincia de Santa Cruz, Argentina. Rev. Asoc. Geol. Argent. 63 (4), 653–664.

Thornber, M.R., 1985. Supergene alteration of sulphides. VII. Distribution of elements during the gossan-forming process. Chem. Geol. 53, 279–301.

Velde, B., 1985. Clay minerals: a physico-chemical explanation of their occurrence: Developments in Sedimentology, 40. Elsevier, Amsterdam, p. 427.

Viera, R., Pezzuchi, H., 1976. Presencia de sedimentitas pérmicas en contacto con rocas

del Complejo metamórfico de la Patagonia extrandina, Ea. Dos Hermanos, provincia de Santa Cruz. Rev. Asoc. Geol. Argent. 31 (4), 281–283.
Wallier, S., 2009. The Geology and Evolution of the Manantial Espejo Epithermal Silver (-Gold) Deposit, Deseado Massif, Argentina. University of British Columbia, Vancouver, Canada. Ph.D. thesis.
Woodcock, N.H., Dickson, J.A.D., Tarasewicz, J.P.T., 2007. Transient permeability and reseal hardening in fault zones: evidence from dilation breccia textures. Geol. Soc. Lond., Spec. Publ. 270, 43–53.